SIAM J. SCI. COMPUT.
Vol. 41, No. 5, pp. A3152–A3181




# EXTENDED MULTIDIMENSIONAL INTEGRATION FORMULAS ON POLYTOPE MESHES*

ALLAL GUESSAB† AND BORIS SEMISALOV‡

**Abstract.** In this paper, we consider a general decomposition of any convex polytope $P \subset \mathbb{R}^n$ into a set of subpolytopes $\Omega_i$ and develop methods for approximating a definite integral of a given function $f$ over $P$ when, rather than its values at some points, a number of integrals of $f$ over the faces of $\Omega_i$ are only available. We present several new families of extended integration formulas that contain such integrals and provide in a special case of our result the multivariate analogues of midpoint, trapezoidal, Hammer, and Simpson rules. The paper also presents the best possible explicit constants for their approximation errors. Here we succeed in finding the connection between minimization of the global error estimate and construction of centroidal Voronoi tessellations of a given polytope with special density function depending on properties of the integrand. In the case of integrands with strong singularities, it leads to essential reduction of the error. These ideas were extended to a more general case, in which the domain is not necessary polytope and is not necessary convex. We perform numerical tests with integrands having steep gradients which allow the comparison of the new cubature formulas and show their accuracy and rates of convergence.

**Key words.** cubature formulas, approximation, convexity, best error estimates, centroidal Voronoi tessellation, singularity of integrand

**AMS subject classifications.** 68Q25, 68R10, 68U05

**DOI.** 10.1137/18M1234564

## 1. Introduction.

Numerical integration of a function $f$ using certain facets, or, most generally, some prescribed hyperplane sections generated by a general decomposition (not necessary simplicial) of a polytope $P$ in $\mathbb{R}^n$, is required in various computational methods. Three notable examples are the discontinuous Galerkin method (see, e.g., [13]), the edge-oriented jump-stabilization method (see [15]), and the nonconforming finite element methods (see, e.g., [3, 2, 1, 12, 7]). It also is needed in tomography and inverse problems: the X-rays of a polytope can be used to estimate the moments of the underlying mass distribution. One can reconstruct any convex polytope from knowledge of its moments. Efficient numerical integration for these approximation methods is often needed to get accurate results. For completeness, let us mention that some numerical integration methods of this type have been recently presented in [4, 10, 11, 5, 14]. However, papers [4, 10, 11] were limited and focused on simplicial or rectangular meshes, and the works [14, 5] only provided a method for the numerical integration of *homogeneous* functions over convex and nonconvex polygons and polyhedra. But the main question remained open in the context of polytope meshes (not necessary simplicial), and research into answering it seems to be missing in the literature. Obviously, for the case of a domain with complex geometry—here an arbitrary polytope (not necessary convex and/or with possible holes)—a triangular mesh is preferred over a rectangular one. However, in certain situations, quadrilateral or, more generally, polytope meshes are preferred in mesh generation practice (both

*Submitted to the journal's Methods and Algorithms for Scientific Computing section December 20, 2018; accepted for publication (in revised form) July 17, 2019; published electronically October 15, 2019.

https://doi.org/10.1137/18M1234564

†Laboratoire de Mathématiques et de leurs Applications, UMR CNRS 4152, Université de Pau et des Pays de l'Adour, 64000 Pau, France (allal.guessab@univ-pau.fr).

‡Novosibirsk State University, 630090, Novosibirsk, Russia, and Institute of Computational Technologies, SB RAS, 630090, Novosibirsk, Russia (vibis87@gmail.com).

because fewer are typically needed and because they have better numerical properties). Hence, our future collaborative work can be viewed as an extension of our joint papers [10, 11] to more general polytope meshes. We should mention also that currently there are only a few multidimensional integration formulas which use integrals over the facets of the mesh. Most of them are dedicated to rectangular meshes and can be regarded as cubature formulas constructed from a tensor product of simple one-dimensional quadratures, which are usually too costly in high dimensions since the number of function calls increases exponentially with the dimension; see [4] and the references given there.

The problem at hand is to numerically evaluate the integral:

$$I(f) := \int_P f(\boldsymbol{x})\ d\boldsymbol{x}, \tag{1.1}$$

where $f : P \to \mathbb{R}$ is an integrable function defined over an arbitrary convex polytope $P \subset \mathbb{R}^n$. We specialize to the particular cases when a number of integrals of $f$ over some hyperplane sections generated by a general decomposition (not necessary simplicial) of a polytope $P$ in $\mathbb{R}^n$ is only available. Let us fix the main idea of our work, its implications, and it applications. As a first step we consider a (conforming) decomposition (also called mesh or grid) $\mathcal{T}$ of $P$, which is a set of subpolytopes $\Omega$ such that

$$\cup_{\Omega\in\mathcal{T}}\Omega = P \ \text{ and } \ \mathring{\Omega}_i \cap \mathring{\Omega}_j = \emptyset,\ i \neq j,$$

where $\Omega_i$, $\Omega_j$ are different subpolytopes in $\mathcal{T}$. Now, (1.1) becomes

$$I(f) = \int_P f(\boldsymbol{x})\ d\boldsymbol{x} = \sum_{\Omega\in\mathcal{T}} \int_\Omega f(\boldsymbol{x})\ d\boldsymbol{x}.$$

Hence, from the above formula, our method for integrating functions over arbitrary polytopes reduces to the problem of constructing accurate numerical integration over every subpolytope $\Omega$ in $\mathcal{T}$. We assume that $\Omega$ has $m$ faces, and it is given as the set of solutions of a finite system of linear inequalities:

$$\Omega = \{\boldsymbol{x} \in \mathbb{R}^n : A\boldsymbol{x} \leq \boldsymbol{b}\},$$

where $A$ is an $m \times n$ matrix of real numbers, and $\boldsymbol{b}$ is a vector of $\mathbb{R}^m$. Let

$$F_i = \{\boldsymbol{x} \in \mathbb{R}^n : A\boldsymbol{x} \leq \boldsymbol{b}, \langle \boldsymbol{a}_i, \boldsymbol{x}\rangle = \boldsymbol{b}_i\},$$

i.e., $F_i$ is the $(n-1)$-dimensional face of $\Omega$ determined by the hyperplane $\langle \boldsymbol{a}_i, \boldsymbol{x}\rangle = \boldsymbol{b}_i$, where $\boldsymbol{a}_i$ is the $i$th row of the matrix $A$. Let $H_i$ denote the $(n-1)$-dimensional affine variety that contains $F_i$. The algebraic distance from the point $\boldsymbol{x}^* \in \mathbb{R}^n$ to $H_i$ is denoted by $d(\boldsymbol{x}^*, H_i)$, and it is given by

$$d(\boldsymbol{x}^*, H_i) = \frac{\boldsymbol{b}_i - \langle \boldsymbol{a}_i, \boldsymbol{x}^*\rangle}{\|\boldsymbol{a}_i\|},$$

where $\|.\|$ is the usual Euclidean norm and $\langle \boldsymbol{x}, \boldsymbol{y}\rangle$ is the standard inner product of $\boldsymbol{x}$ and $\boldsymbol{y}$. Further, for simplicity we shall use the notation "$d(\boldsymbol{x}^*, F_i)$" instead of "$d(\boldsymbol{x}^*, H_i)$." The $n$-dimensional (resp., $(n-1)$-dimensional) volume of $\Omega$ (resp., $F_i$) is denoted by $V_n(\Omega)$ (resp., by $V_{n-1}(F_i)$).

**2. A multivariate analogue of trapezoidal rule and its consequences.** Henceforth, we shall let $\boldsymbol{c}_\Omega$ denote the center of gravity of $\Omega$. Under the assumption that the density of $P$ is uniform, it is defined as

$$\boldsymbol{c}_\Omega = \frac{\int_\Omega \boldsymbol{x}\, d\boldsymbol{x}}{V_n(\Omega)}. \tag{2.1}$$

Let $\nabla f(\boldsymbol{x})$ denote the gradient of $f$ at $\boldsymbol{x}$. We now introduce the Green's formula, which can be stated as (see [6])

$$\int_\Omega f(\boldsymbol{x})\triangle u(\boldsymbol{x})\, d\boldsymbol{x} + \int_\Omega \langle\, \nabla f(\boldsymbol{x}), \nabla u(\boldsymbol{x})\rangle d\boldsymbol{x} = \sum_{i=1}^{m} \int_{F_i} f(\boldsymbol{x})\langle\, \nabla u(\boldsymbol{x}), \boldsymbol{n}_i\rangle\, d\gamma_i, \tag{2.2}$$

where $d\gamma_i$ is the element of integration over $F_i$, and

$$\triangle = \frac{\partial^2}{\partial x_1^2} + \cdots + \frac{\partial^2}{\partial x_n^2}$$

is the Laplace operator. Formula (2.2) is valid for any twice continuously differentiable function $u$ and for any continuously differentiable function $f$. Here $\boldsymbol{n}_i$ is the unit outward-pointing normal to $F_i$. If we take

$$u(\boldsymbol{x}) = \frac{\|\boldsymbol{x} - \boldsymbol{c}_\Omega\|^2}{2},$$

then the following identities hold true for all $\boldsymbol{x} \in F_i$:

$$\begin{aligned} \triangle u(\boldsymbol{x}) &= n, \\ \nabla u(\boldsymbol{x}) &= \boldsymbol{x} - \boldsymbol{c}_\Omega. \end{aligned}$$

Moreover, we also know that $\boldsymbol{n}_i = \frac{\boldsymbol{a}_i}{\|\boldsymbol{a}_i\|}$. This is readily verified by normalizing the gradient of $\langle \boldsymbol{a}_i, \boldsymbol{x}\rangle$, which is in the direction that is perpendicular to the isocontours of $\langle \boldsymbol{a}_i, \boldsymbol{x}\rangle$. Hence, it must also hold true that

$$\langle\, \nabla u(\boldsymbol{x}), \boldsymbol{n}_i\rangle = \langle\, \boldsymbol{x} - \boldsymbol{c}_\Omega, \boldsymbol{n}_i\rangle = \frac{\langle \boldsymbol{x}, \boldsymbol{a}_i\rangle - \langle \boldsymbol{a}_i, \boldsymbol{c}_\Omega\rangle}{\|\boldsymbol{a}_i\|} = \frac{\boldsymbol{b}_i - \langle \boldsymbol{a}_i, \boldsymbol{c}_\Omega\rangle}{\|\boldsymbol{a}_i\|}.$$

Furthermore, in view of the fact that

$$d(\boldsymbol{c}_\Omega, F_i) = \frac{\boldsymbol{b}_i - \langle \boldsymbol{a}_i, \boldsymbol{c}_\Omega\rangle}{\|\boldsymbol{a}_i\|},$$

we therefore get the identity

$$\langle\, \nabla u(\boldsymbol{x}), \boldsymbol{n}_i\rangle = d(\boldsymbol{c}_\Omega, F_i) \quad (i = 1, \ldots, m).$$

Hence, (2.2) reduces to

$$\begin{aligned} n\int_\Omega f(\boldsymbol{x})\, d\boldsymbol{x} + \int_\Omega \langle\, \nabla f(\boldsymbol{x}), \boldsymbol{x} - \boldsymbol{c}_\Omega\rangle d\boldsymbol{x} &= \sum_{i=1}^{m} \int_{F_i} \langle\, \boldsymbol{x} - \boldsymbol{c}_\Omega, \boldsymbol{n}_i\rangle f(\boldsymbol{x}) d\gamma_i \\ &= \sum_{i=1}^{m} d(\boldsymbol{c}_\Omega, F_i) \int_{F_i} f(\boldsymbol{x}) d\gamma_i. \end{aligned} \tag{2.3}$$

This can be written in the following more convenient form:

$$\int_\Omega f(\boldsymbol{x})\,d\boldsymbol{x} + \frac{1}{n}\int_\Omega \langle\,\nabla f(\boldsymbol{x}), \boldsymbol{x}-\boldsymbol{c}_\Omega\rangle d\boldsymbol{x} = \sum_{i=1}^{m} \frac{d(\boldsymbol{c}_\Omega, F_i)}{n}\int_{F_i} f(\boldsymbol{x}) d\gamma_i. \tag{2.4}$$

We shall consider the following approximate formula for integration of functions over subpolytope $\Omega$. It is defined as follows:

$$\int_\Omega f(\boldsymbol{x})\,d\boldsymbol{x} \approx Q_\Omega^{\mathrm{tra}}(f),$$

where

$$Q_\Omega^{\mathrm{tra}}(f) = \sum_{i=1}^{m} \frac{d(\boldsymbol{c}_\Omega, F_i)}{n}\int_{F_i} f(\boldsymbol{x}) d\gamma_i. \tag{2.5}$$

This (extended) cubature formula may thus be considered as a multivariate version of the classical trapezoidal rule, since in the one-dimensional case $Q_\Omega^{\mathrm{tra}}$ reduces to the latter. Recall that the formula for the trapezoid rule is

$$\int_a^b f(x)\,dx \approx Q_{[a,b]}^{\mathrm{tra}}(f) = (b-a)\frac{f(a)+f(b)}{2}.$$

As in the one-dimensional case, the following result shows that the extended cubature formula (2.5) is exact for affine functions over $\Omega$.

LEMMA 2.1. *Let $f$ be an affine function on $\Omega$; then the following identity holds:*

$$\int_\Omega f(\boldsymbol{x})\,d\boldsymbol{x} = Q_\Omega^{\mathrm{tra}}(f) = \sum_{i=1}^{m} \frac{d(\boldsymbol{c}_\Omega, F_i)}{n}\int_{F_i} f(\boldsymbol{x}) d\gamma_i. \tag{2.6}$$

*Proof.* Let us first observe that the center of gravity $\boldsymbol{c}_\Omega$ of $\Omega$ satisfies

$$\boldsymbol{c}_\Omega = \frac{1}{V_n(\Omega)}\int_\Omega \boldsymbol{x}\,d\boldsymbol{x} \text{ or } \int_\Omega (\boldsymbol{x}-\boldsymbol{c}_\Omega)\,d\boldsymbol{x} = \boldsymbol{0}. \tag{2.7}$$

Now, let $f$ be an affine function on $\Omega$. Since the gradient is constant for any affine function, then by (2.7) we get

$$\int_\Omega \langle\,\nabla f(\boldsymbol{x}), \boldsymbol{x}-\boldsymbol{c}_\Omega\rangle d\boldsymbol{x} = \left\langle\,\nabla f(\boldsymbol{x}), \int_\Omega (\boldsymbol{x}-\boldsymbol{c}_\Omega)\,d\boldsymbol{x}\right\rangle = 0. \tag{2.8}$$

Hence, if $f$ is affine, then by (2.8) the Green's formula (2.4) simplifies to

$$\int_\Omega f(\boldsymbol{x})\,d\boldsymbol{x} = \sum_{i=1}^{m} \frac{d(\boldsymbol{c}_\Omega, F_i)}{n}\int_{F_i} f(\boldsymbol{x}) d\gamma_i,$$

showing that the required statement (2.6) holds for any affine function. ∎

With regards to Lemma 2.1, we now ask the following question.

QUESTION 2.2. *Under which condition does equality* (2.6) *of Lemma* 2.1 *continue to hold?*

We can also ask a more general question about the following one-sided approximation from above.

QUESTION 2.3. *Under which condition does the inequality*

$$\int_\Omega f(\boldsymbol{x})\,d\boldsymbol{x} \le Q_\Omega^{\mathrm{tra}}(f) = \sum_{i=1}^{m} \frac{d(\boldsymbol{c}_\Omega, F_i)}{n} \int_{F_i} f(\boldsymbol{x}) d\gamma_i \tag{2.9}$$

*hold?*

Let us first answer Question 2.3. In doing so, we establish a characterization of functions for which our multivariate version of the trapezoidal rule approximates them from above. Let us state this explicitly.

THEOREM 2.4. *Let $f$ be a continuously differentiable function on $\Omega$; then the following two statements are equivalent:*

(i) *$f$ satisfies* (2.9).

(ii) *$f$ satisfies*

$$\int_\Omega \langle \nabla f(\boldsymbol{x}) - \nabla f(\boldsymbol{c}_\Omega), \boldsymbol{x} - \boldsymbol{c}_\Omega \rangle\, d\boldsymbol{x} \ge 0. \tag{2.10}$$

*Equality occurs in* (2.9) *and* (2.10) *for affine functions.*

*Proof.* In view of (2.7), identity (2.4) can be transformed as follows:

$$\begin{aligned} &\int_\Omega f(\boldsymbol{x})\,d\boldsymbol{x} + \frac{1}{n}\int_\Omega \langle \nabla f(\boldsymbol{x}) - \nabla f(\boldsymbol{c}_\Omega), \boldsymbol{x} - \boldsymbol{c}_\Omega \rangle d\boldsymbol{x} \\ &\qquad = \sum_{i=1}^{m} \frac{d(\boldsymbol{c}_\Omega, F_i)}{n} \int_{F_i} f(\boldsymbol{x}) d\gamma_i, \end{aligned} \tag{2.11}$$

and the conclusion of the theorem is obvious. ∎

We are now ready to answer Question 2.2. Indeed, as a consequence of identity (2.11), we provide a characterization result for functions which satisfy equality (2.6). This result can also be applied to give another proof of Lemma 2.1 via identity (2.12).

COROLLARY 2.5. *Let $f$ be a continuously differentiable function on $\Omega$; then the following two statements are equivalent:*

(i) *$f$ satisfies* (2.6).

(ii) *$f$ satisfies*

$$\int_\Omega \langle \nabla f(\boldsymbol{x}) - \nabla f(\boldsymbol{c}_\Omega), \boldsymbol{x} - \boldsymbol{c}_\Omega \rangle\, d\boldsymbol{x} = 0. \tag{2.12}$$

The next corollary furnishes a large class of functions which satisfy inequality (2.9). Indeed, using the monotonicity of the gradient, we see that the second integral in (2.11) is nonnegative for any continuously differentiable convex function on $\Omega$; then the following result is an immediate consequence of (2.11).

COROLLARY 2.6. *For any continuously differentiable convex function $f$ on $\Omega$, inequality* (2.9) *holds. Moreover, the equality in* (2.9) *is attained if $f$ satisfies* (2.12).

Let us introduce the following approximate formula for integration of functions over subpolytope $\Omega$:

$$\int_\Omega f(\boldsymbol{x})\,d\boldsymbol{x} \approx Q_\Omega^{\mathrm{mid}}(f) = V_n(\Omega) f(\boldsymbol{c}_\Omega). \tag{2.13}$$

It should be observed that $Q_\Omega^{\mathrm{mid}}$ can be seen as a multivariate version of the midpoint rule. Following Theorem 2.1 from [9] for any convex function $f$, we can write

$$Q_\Omega^{\mathrm{mid}}(f) \leq \int_\Omega f(\boldsymbol{x})\, d\boldsymbol{x}. \tag{2.14}$$

The equality in (2.14) is attained if and only if $f$ is affine.

Now, we define another cubature formula $Q_\Omega^{\mathrm{Ha}}$ as follows:

$$\int_\Omega f(\boldsymbol{x})\, d\boldsymbol{x} \approx Q_\Omega^{\mathrm{Ha}}(f) = \frac{1}{n+1} Q_\Omega^{\mathrm{mid}}(f) + \frac{n}{n+1} Q_\Omega^{\mathrm{tra}}(f), \tag{2.15}$$

where $Q_\Omega^{\mathrm{tra}}$ and $Q_\Omega^{\mathrm{mid}}$ are defined as in (2.5) and (2.13), respectively.

The following result shows that the cubature formula $Q_\Omega^{\mathrm{Ha}}$ as defined in (2.15) is exact for affine functions over $\Omega$.

LEMMA 2.7. *Let $f$ be an affine function on $\Omega$; then the following identity holds:*

$$\begin{aligned}\int_\Omega f(\boldsymbol{x})\, d\boldsymbol{x} &= Q_\Omega^{\mathrm{Ha}}(f) \\ &= \frac{V_n(\Omega)}{n+1} f(\boldsymbol{c}_\Omega) + \frac{n}{n+1} \sum_{i=1}^{m} \frac{d(\boldsymbol{c}_\Omega, F_i)}{n} \int_{F_i} f(\boldsymbol{x}) d\gamma_i.\end{aligned}$$

*Proof.* Theorem 2.1 from [9] shows that the multivariate midpoint formula $Q_\Omega^{\mathrm{mid}}$ is exact for any affine function. Finally, by Lemma 2.1 we know already that $Q_\Omega^{\mathrm{tra}}$ is also exact for affine functions, as $Q_\Omega^{\mathrm{Ha}}$ is a convex combination of $Q_\Omega^{\mathrm{mid}}$ and $Q_\Omega^{\mathrm{tra}}$; then the required result follows. ∎

*Remark* 2.8. Let us emphasis that by virtue of Lemma 2.1, Theorem 2.1 from [9], and Lemma 2.7 the trapezoidal, midpoint, and Hammer rules are exact on affine functions. Therefore, we can conclude that they have at least the second order of convergence.

With regards to Lemma 2.7, we now ask the following question about the one-sided approximation of $Q_\Omega^{\mathrm{Ha}}$.

QUESTION 2.9. *Under which conditions on $f$ does the inequality*

$$\int_\Omega f(\boldsymbol{x})\, d\boldsymbol{x} \leq Q_\Omega^{\mathrm{Ha}}(f) = \frac{V_n(\Omega)}{n+1} f(\boldsymbol{c}_\Omega) + \frac{n}{n+1} \sum_{i=1}^{m} \frac{d(\boldsymbol{c}_\Omega, F_i)}{n} \int_{F_i} f(\boldsymbol{x}) d\gamma_i \tag{2.16}$$

*hold?*

We next show a necessary and sufficient condition in order that the one-sided approximation (2.16) holds.

THEOREM 2.10. *Let $f$ be a continuously differentiable function on convex $\Omega$; then the following three statements are equivalent:*

(i) *$f$ satisfies inequality* (2.16).

(ii) *$f$ satisfies*

$$\begin{aligned}E^{\mathrm{mid}}(f) &:= \int_\Omega f(\boldsymbol{x})\, d\boldsymbol{x} - V_n(\Omega) f(\boldsymbol{c}_\Omega) \\ &\leq \int_\Omega \langle \nabla f(\boldsymbol{x}) - \nabla f(\boldsymbol{c}_\Omega), \boldsymbol{x} - \boldsymbol{c}_\Omega \rangle\, d\boldsymbol{x}.\end{aligned} \tag{2.17}$$

(iii) *$f$ is convex.*

*Equality occurs in* (2.16) *and* (2.17) *for affine functions.*

*Proof.* First, observe that the Green's formula as described in (2.3) may be reformulated as

$$(n+1)\int_\Omega f(\boldsymbol{x})\,d\boldsymbol{x} + \int_\Omega (\langle \nabla f(\boldsymbol{x}) - \nabla f(\boldsymbol{c}_\Omega), \boldsymbol{x}-\boldsymbol{c}_\Omega\rangle - f(\boldsymbol{x}) + f(\boldsymbol{c}_\Omega))d\boldsymbol{x} = V_n(\Omega) f(\boldsymbol{c}_\Omega) + \sum_{i=1}^m d(\boldsymbol{c}_\Omega, F_i)\int_{F_i} f(\boldsymbol{x}) d\gamma_i,$$

or equivalently, after some simplification, as

$$\int_\Omega f(\boldsymbol{x})\,d\boldsymbol{x} + \frac{1}{n+1}\int_\Omega \left(\langle \nabla f(\boldsymbol{x}) - \nabla f(\boldsymbol{c}_\Omega), \boldsymbol{x}-\boldsymbol{c}_\Omega\rangle - E_\Omega^{\mathrm{mid}}(f)\right) d\boldsymbol{x} = Q_\Omega^{\mathrm{Ha}}. \tag{2.18}$$

This yields the equivalence of (i) and (ii).

We also can rewrite the Green's formula in another similar form,

$$(n+1)\int_\Omega f(\boldsymbol{x})\,d\boldsymbol{x} + \int_\Omega (\langle \nabla f(\boldsymbol{x}), \boldsymbol{x}-\boldsymbol{c}_\Omega\rangle - f(\boldsymbol{x}) + f(\boldsymbol{c}_\Omega))d\boldsymbol{x} = V_n(\Omega) f(\boldsymbol{c}_\Omega) + \sum_{i=1}^m d(\boldsymbol{c}_\Omega, F_i)\int_{F_i} f(\boldsymbol{x}) d\gamma_i,$$

and get

$$Q_\Omega^{\mathrm{Ha}} - \int_\Omega f(\boldsymbol{x})\,d\boldsymbol{x} = \frac{1}{n+1}\int_\Omega \left(f(\boldsymbol{c}_\Omega) - f(\boldsymbol{x}) + \langle \nabla f(\boldsymbol{x}), \boldsymbol{x}-\boldsymbol{c}_\Omega\rangle\right) d\boldsymbol{x}. \tag{2.19}$$

The first order condition for convexity (gradient inequality) tells us that function $f$ is convex on $\Omega$ if and only if for any points $\boldsymbol{x}$ and $\boldsymbol{y}$ in $\Omega$

$$f(\boldsymbol{y}) \geq f(\boldsymbol{x}) + \langle \nabla f(\boldsymbol{x}), \boldsymbol{y}-\boldsymbol{x}\rangle$$

or equivalently, by taking $y = \boldsymbol{c}_\Omega$,

$$f(\boldsymbol{c}_\Omega) - f(\boldsymbol{x}) + \langle \nabla f(\boldsymbol{x}), \boldsymbol{x}-\boldsymbol{c}_\Omega\rangle \geq 0.$$

Together with equality (2.19) this means that (i) and (iii) are equivalent. ∎

Finally we introduce another cubature formula that is a multivariate version of the Simpson rule for integration of functions over subpolytope $\Omega$. It is a convex combination of the described multivariate versions of the midpoint and trapezoidal rules:

$$\int_\Omega f(\boldsymbol{x})\,d\boldsymbol{x} \approx Q_\Omega^{\mathrm{Si}}(f),$$

with

$$Q_\Omega^{\mathrm{Si}}(f) = \frac{2}{n+2} Q_\Omega^{\mathrm{mid}}(f) + \frac{n}{n+2} Q_\Omega^{\mathrm{tra}}(f), \tag{2.20}$$

where $Q_\Omega^{\mathrm{mid}}$ and $Q_\Omega^{\mathrm{tra}}$ are given by (2.13) and (2.5), respectively. Recall that in the one-dimensional case, the Simpson rule can be expressed on the interval $[a,b]$ as

$$\frac{1}{b-a}\int_a^b f(t)dt = \frac{2}{3} f\left(\frac{a+b}{2}\right) + \frac{1}{3}\left(\frac{f(a)+f(b)}{2}\right) + E^{\mathrm{Si}}[f]. \tag{2.21}$$

Hence, the cubature formula (2.20) appears as a natural extension to higher dimensions of the classical Simpson rule. In the one-dimensional case, the Simpson rule has the fourth order of convergence to the exact value of the integral. The Simpson cubature formula as defined in (2.20) has order greater than 2. Indeed, the following theorem holds.

PROPOSITION 2.11. *Consider the integration formula*

$$\int_\Omega f(\boldsymbol{x})\,d\boldsymbol{x} = \frac{2}{n+2}Q_\Omega^{\mathrm{mid}}(f) + \frac{n}{n+2}Q_\Omega^{\mathrm{tra}}(f) + R_\Omega^{\mathrm{Si}}(f).$$

*Then* $R_\Omega^{\mathrm{Si}}(f) = 0$ *whenever* $f$ *is a polynomial in* $d$ *variables of total degree at most two.*

*Proof.* Since $Q_\Omega^{\mathrm{mid}}$ and $Q_\Omega^{\mathrm{tra}}$ are exact for affine functions, then by linearity of $R_\Omega^{\mathrm{Si}}$ it is enough to verify that $R_\Omega^{\mathrm{Si}}(f) = 0$ for the following monomials:

$$f(\boldsymbol{x}) = x_j x_k, \quad j,k = 1,\dots,n, j \neq k,$$

and

$$g(\boldsymbol{x}) = x_j^2, \quad j = 1,\dots,n.$$

Applying the Green's formula (2.11) to $f$ gives

$$\int_\Omega x_j x_k\,d\boldsymbol{x} = Q_\Omega^{\mathrm{tra}}(x_j x_k) - \frac{2}{n}\int_\Omega (x_j - c_{\Omega,j})(x_k - c_{\Omega,k})\,d\boldsymbol{x}. \tag{2.22}$$

Moreover a simple calculation leads to

$$\int_\Omega (x_j - c_{\Omega,j})(x_k - c_{\Omega,k})\,d\boldsymbol{x} = \int_\Omega x_j x_k\,d\boldsymbol{x} - Q_\Omega^{\mathrm{mid}}(x_j x_k).$$

Multiplying both sides of the last equation by $-\frac{2}{n}$ and adding (2.22), we arrive at

$$\frac{n+2}{n}\int_\Omega x_j x_k\,d\boldsymbol{x} = Q_\Omega^{\mathrm{tra}}(x_j x_k) + \frac{2}{n}Q_\Omega^{\mathrm{mid}}(x_j x_k).$$

Multiplying therefore the right-hand side of the last equation by $\frac{n}{n+2}$, we obtain

$$R_\Omega^{\mathrm{Si}}(x_j x_k) = 0, \quad j,k = 1,\dots,n, j \neq k. \tag{2.23}$$

Similarly, applying again the Green's formula (2.11) to $g$, we get the identities

$$\int_\Omega x_j^2\,d\boldsymbol{x} = Q_\Omega^{\mathrm{tra}}(x_j^2) - \frac{2}{n}\int_\Omega (x_j - c_{\Omega,j})^2\,d\boldsymbol{x} \tag{2.24}$$

and

$$\int_\Omega (x_j - c_{\Omega,j})^2\,d\boldsymbol{x} = \int_\Omega x_j^2\,d\boldsymbol{x} - Q_\Omega^{\mathrm{mid}}(x_j^2).$$

Hence, plugging this into (2.24) gives

$$R_\Omega^{\mathrm{Si}}(x_j^2) = 0, \quad j = 1,\dots,n. \tag{2.25}$$

The previous identities, together with (2.23), show that the desired result holds. ∎

*Remark* 2.12. Cubature formulas of high order of approximation of the type considered in this paper are currently being made and will be the object of a forthcoming paper.

**3. Best cubature error bounds.**

**3.1. Characterization of cubature formulas that satisfy an upper or a lower Hermite–Hadamard inequality.** Let $H_i, i = 1, \dots, m$, be certain hyperplane sections of a subpolytope $\Omega$ that are only available. Error estimates are established for numerical integration formulas of type

$$\frac{1}{|\Omega|}\int_\Omega f(\boldsymbol{x})\,d\boldsymbol{x} = \sum_{i=1}^{m}\omega_i \int_{F_i} f\,d\gamma_i + E(f),$$

which are assumed to satisfy an upper or a lower Hermite–Hadamard inequality for any convex function. This means that $E(f) \geq 0$ (or, respectively, $E(f) \leq 0$) for any convex function; see [9]. Note that, as shown by inequality (2.14) and by Corollary 2.6, the formulas $Q_\Omega^{\mathrm{mid}}(f)$ and $Q_\Omega^{\mathrm{tra}}(f)$ satisfy these conditions correspondingly. Also according to Theorem 2.10 condition $E(f) \leq 0$ can be satisfied by using $Q_\Omega^{\mathrm{Ha}}(f)$.

Our main goal here is to estimate the error $E(f)$, assuming that $f$ is a differentiable function with Lipschitz continuous gradient. Let us now introduce the functional spaces under consideration.

DEFINITION 3.1. *A differentiable function $f : \Omega \to \mathbb{R}$ is said to have a Lipschitz continuous gradient if there exists a real positive constant $\rho(\nabla f)$, such that*

$$\|\nabla f(\boldsymbol{x}) - \nabla f(\boldsymbol{y})\| \leq \rho(\nabla f)\,\|\boldsymbol{x} - \boldsymbol{y}\| \quad (\boldsymbol{x}, \boldsymbol{y} \in \Omega). \tag{3.1}$$

For any differentiable $f$ with Lipschitz continuous gradient there exists a smallest possible $\rho(\nabla f)$ such that (3.1) holds. The smallest constant $L(\nabla f) := Lip(\nabla f)$ satisfying inequality (3.1) is called the Lipschitz constant for $\nabla f$. We shall denote by $C^{1,1}(\Omega)$ the subclass of all functions $f$ which are continuously differentiable on $\Omega$ with Lipschitz continuous gradients.

For a cubature formula which satisfies an upper or a lower Hermite–Hadamard inequality, its approximation error is characterized as follows. We state the following theorem without proof since a simple inspection of results in [11] may reveal that their extension given here holds for any polytope (not just simplices).

THEOREM 3.2. *Let $H_i, i = 1, \dots, m$, be some given hyperplane sections of the subpolytope $\Omega$ with positive measures. Define the integration formula via*

$$\int_\Omega f(\boldsymbol{x})\,d\boldsymbol{x} = \sum_{i=1}^{m}\omega_i \int_{H_i} f\,d\gamma_i + E(f),$$

*where $d\gamma_i$ is the element of integration over $H_i$, and let $\epsilon \in \{-1, 1\}$. Then the following two statements are equivalent:*

(i) *For every convex function $g \in C^{1,1}(\Omega)$, we have*

$$\epsilon E\,[g] \geq 0.$$

(ii) *For every $f \in C^{1,1}(\Omega)$ with $L(\nabla f)$-Lipschitz gradient, we have*

$$|E\,[f]\,| \leq \epsilon E\left[\|.\|^2\right]\frac{L(\nabla f)}{2}.$$

*Equality is attained for all functions of the form*

$$f(\boldsymbol{x}) := a(\boldsymbol{x}) + c\|.\|^2,$$

*where $c \in \mathbb{R}$ and $a(\cdot)$ is any affine function.*

**3.2. Local error estimates.** As announced in the introduction, we are now in a position to derive the following explicit sharp bounds for the approximation errors.

THEOREM 3.3. *Let $f \in C^{1,1}(P)$ have an $L(\nabla f)$-Lipschitz gradient, and let the cubature formulas be given as in* (2.5), (2.13), *and* (2.15). *Then the following error estimates hold:*

$$\left|E_\Omega^{\mathrm{tra}}(f)\right| \leq \frac{L(\nabla f)}{n} \int_\Omega \|\boldsymbol{x} - \boldsymbol{c}_\Omega\|^2 \, d\boldsymbol{x},$$

$$\left|E_\Omega^{\mathrm{mid}}(f)\right| \leq \frac{L(\nabla f)}{2} \int_\Omega \|\boldsymbol{x} - \boldsymbol{c}_\Omega\|^2 \, d\boldsymbol{x},$$

$$\left|E_\Omega^{\mathrm{Ha}}(f)\right| \leq \frac{L(\nabla f)}{2(n+1)} \int_\Omega \|\boldsymbol{x} - \boldsymbol{c}_\Omega\|^2 \, d\boldsymbol{x}.$$

*Proof.* According to the discussion above and Theorem 3.2, it will suffice to show that

$$\left|E_\Omega^{\mathrm{tra}}(\|.\|^2)\right| = \frac{2}{n} \int_\Omega \|\boldsymbol{x} - \boldsymbol{c}_\Omega\|^2 \, d\boldsymbol{x}, \tag{3.2}$$

$$\left|E_\Omega^{\mathrm{mid}}(\|.\|^2)\right| = \int_\Omega \|\boldsymbol{x} - \boldsymbol{c}_\Omega\|^2 \, d\boldsymbol{x}, \tag{3.3}$$

$$\left|E_\Omega^{\mathrm{Ha}}(\|.\|^2)\right| = \frac{1}{n+1} \int_\Omega \|\boldsymbol{x} - \boldsymbol{c}_\Omega\|^2 \, d\boldsymbol{x}. \tag{3.4}$$

To prove identity (3.2), we use (2.11) and $f(\boldsymbol{x}) = \|\boldsymbol{x}\|^2$ to get

$$\begin{aligned}\int_\Omega \|\boldsymbol{x}\|^2 \, d\boldsymbol{x} - \sum_{i=1}^m \frac{d(\boldsymbol{c}_\Omega, F_i)}{n} \int_{F_i} \|\boldsymbol{x}\|^2 \, d\gamma_i &= -\frac{2}{n} \int_\Omega \langle \boldsymbol{x} - \boldsymbol{c}_\Omega, \boldsymbol{x} - \boldsymbol{c}_\Omega \rangle d\boldsymbol{x} \\ &= -\frac{2}{n} \int_\Omega \|\boldsymbol{x} - \boldsymbol{c}_\Omega\|^2 \, d\boldsymbol{x}.\end{aligned}$$

In order to prove (3.3), we proceed as follows:

$$\begin{aligned}\int_\Omega \|\boldsymbol{x} - \boldsymbol{c}_\Omega\|^2 \, d\boldsymbol{x} &= \int_\Omega \langle \boldsymbol{x} - \boldsymbol{c}_\Omega, \boldsymbol{x} - \boldsymbol{c}_\Omega \rangle d\boldsymbol{x} \\ &= \int_\Omega \langle \boldsymbol{x}, \boldsymbol{x} - \boldsymbol{c}_\Omega \rangle d\boldsymbol{x} - \int_\Omega \langle \boldsymbol{c}_\Omega, \boldsymbol{x} - \boldsymbol{c}_\Omega \rangle d\boldsymbol{x} \\ &= \int_\Omega \langle \boldsymbol{x}, \boldsymbol{x} - \boldsymbol{c}_\Omega \rangle d\boldsymbol{x} \\ &= \int_\Omega \langle \boldsymbol{x}, \boldsymbol{x} \rangle d\boldsymbol{x} - \int_\Omega \langle \boldsymbol{x}, \boldsymbol{c}_\Omega \rangle d\boldsymbol{x} \\ &= \int_\Omega \|\boldsymbol{x}\|^2 \, d\boldsymbol{x} - Q_\Omega^{\mathrm{mid}}(\|\boldsymbol{x}\|^2) = E_\Omega^{\mathrm{mid}}(\|.\|^2). \end{aligned} \tag{3.5}$$

The last equalities in (3.5) are valid since $\boldsymbol{c}_\Omega = \frac{1}{V_n(\Omega)} \int_\Omega \boldsymbol{x} d\boldsymbol{x}$ and therefore

$$\int_\Omega \langle \boldsymbol{x}, \boldsymbol{c}_\Omega \rangle d\boldsymbol{x} = \left\langle \int_\Omega \boldsymbol{x} d\boldsymbol{x}, \boldsymbol{c}_\Omega \right\rangle = \langle V_n(\Omega) \boldsymbol{c}_\Omega, \boldsymbol{c}_\Omega \rangle = V_n(\Omega) \|\boldsymbol{c}_\Omega\|^2.$$

Finally, by using (2.18) applied to $f(\boldsymbol{x}) = \|\boldsymbol{x}\|^2$ we get

$$\int_\Omega \|\boldsymbol{x}\|^2 \, d\boldsymbol{x} - Q_\Omega^{\mathrm{Ha}}(\|.\|^2) = \frac{-1}{n+1} \left( \int_\Omega 2 \|\boldsymbol{x} - \boldsymbol{c}_\Omega\|^2 \, d\boldsymbol{x} - E_\Omega^{\mathrm{mid}}(\|.\|^2) \right).$$

The required identity (3.4) now follows from (3.5). ∎

In the one-dimensional case $n = 1$, we can see that the best constant of the error in the trapezoidal rule is twice as large as that for the midpoint rule. The literature contains a number of variations of this result; some statements employ the largest absolute value of the second derivative over the interval $[a, b]$. Let us also observe that these constants are equal for the case $n = 2$; however, for $n \geq 3$, we have the surprising and interesting fact that the best constant of the error in the midpoint cubature formula is always larger than that for the trapezoidal cubature formula.

Theorem 3.3 also shows that for any $n$, the cubature formula $Q_\Omega^{\mathrm{Ha}}$ has the smallest constant in its error estimate among the three formulas under consideration.

**3.3. Global error estimates.** Now, let $\Omega$ be subpolytopes in the decomposition $\mathcal{T}$ of the polytope $P$. Since

$$\int_P f(\boldsymbol{x})\, d\boldsymbol{x} = \sum_{\Omega\in\mathcal{T}} \int_\Omega f(\boldsymbol{x})\, d\boldsymbol{x}$$

it produces the cubature formulas

$$\int_P f(\boldsymbol{x})\, d\boldsymbol{x} = \sum_{\Omega\in\mathcal{T}} Q_\Omega^{\mathrm{tra}}(f) + E_P^{\mathrm{tra}}(f), \tag{3.6}$$

$$\int_P f(\boldsymbol{x})\, d\boldsymbol{x} = \sum_{\Omega\in\mathcal{T}} Q_\Omega^{\mathrm{mid}}(f) + E_P^{\mathrm{mid}}(f), \tag{3.7}$$

$$\int_P f(\boldsymbol{x})\, d\boldsymbol{x} = \sum_{\Omega\in\mathcal{T}} Q_\Omega^{\mathrm{Ha}}(f) + E_P^{\mathrm{Ha}}(f), \tag{3.8}$$

where the cubature formulas $Q_\Omega^{\mathrm{tra}}$, $Q_\Omega^{\mathrm{mid}}$, and $Q_\Omega^{\mathrm{Ha}}$ are given as in (2.5), (2.13), and (2.15), respectively. The following result is a simple consequence of the definitions of the approximation errors $E_P^{\mathrm{tra}}, E_P^{\mathrm{mid}}, E_P^{\mathrm{Ha}}$ and Theorem 3.3.

THEOREM 3.4. *Let $f \in C^{1,1}(\Omega)$ have an $L(\nabla f)$-Lipschitz gradient. Let the cubature formulas be given as in* (3.6)–(3.8). *Then the following error estimates hold:*

$$\left|E_P^{\mathrm{tra}}(f)\right| \leq \sum_{\Omega\in\mathcal{T}} \frac{L_\Omega(\nabla f)}{n} \int_\Omega \|\boldsymbol{x} - \boldsymbol{c}_\Omega\|^2\, d\boldsymbol{x}, \tag{3.9}$$

$$\left|E_P^{\mathrm{mid}}(f)\right| \leq \frac{1}{2} \sum_{\Omega\in\mathcal{T}} L_\Omega(\nabla f) \int_\Omega \|\boldsymbol{x} - \boldsymbol{c}_\Omega\|^2\, d\boldsymbol{x}, \tag{3.10}$$

$$\left|E_P^{\mathrm{Ha}}(f)\right| \leq \frac{1}{2(n+1)} \sum_{\Omega\in\mathcal{T}} L_\Omega(\nabla f) \int_\Omega \|\boldsymbol{x} - \boldsymbol{c}_\Omega\|^2\, d\boldsymbol{x}. \tag{3.11}$$

In order to minimize the energy functional

$$F_E = \sum_{\Omega\in\mathcal{T}} L_\Omega(\nabla f) \int_\Omega \|\boldsymbol{x} - \boldsymbol{c}_\Omega\|^2\, d\boldsymbol{x}, \tag{3.12}$$

which correlates with the upper bounds of approximation errors, we first present the definition and properties of the *centroidal Voronoi tessellations* (CVTs). More details about CVTs can be found in the survey [8].

Given $k$ points $\boldsymbol{x}_1, \boldsymbol{x}_2, \ldots, \boldsymbol{x}_k$ inside the polytope $P$, the Voronoi diagram is defined as the collection of the Voronoi regions $\Omega_i, i = 1, 2, \ldots, k$, that are defined as

$$\Omega_i = \{\boldsymbol{x} \in P : \|\boldsymbol{x} - \boldsymbol{x}_i\| < \|\boldsymbol{x} - \boldsymbol{x}_j\|, j \neq i\}.$$

The CVT is a special Voronoi diagram in which each generator point $\boldsymbol{x}_i$ coincides with the center of gravity $\boldsymbol{s}_{\Omega_i}$ of its Voronoi region,

$$\boldsymbol{x}_i = \boldsymbol{s}_{\Omega_i} = \frac{\int_{\Omega_i} \mu(\boldsymbol{x}) \boldsymbol{x}\, d\boldsymbol{x}}{\int_{\Omega_i} \mu(\boldsymbol{x})\, d\boldsymbol{x}},$$

where $\mu(\boldsymbol{x})$ is the density function defined on the whole polytope $P$. For the case $\mu(\boldsymbol{x}) \equiv \text{const}$, $\boldsymbol{s}_{\Omega_i} = \boldsymbol{c}_{\Omega_i}$; see (2.1). The CVT energy functional $F$ is defined for the arbitrary set of points $X = \{\boldsymbol{x}_1, \boldsymbol{x}_2, \ldots, \boldsymbol{x}_k\}$ in $P$ as

$$F(X) = \sum_{i=1}^{k} \int_{\Omega_i} \mu(\boldsymbol{x}) \|\boldsymbol{x} - \boldsymbol{x}_i\|^2 d\boldsymbol{x}. \tag{3.13}$$

By [8, Proposition 3.1], a necessary condition for minimizing the last expression is that $\{\Omega_i, i = 1, \ldots, k\}$ is a CVT generated by $\{\boldsymbol{x}_i = \boldsymbol{s}_{\Omega_i}, i = 1, \ldots, k\}$. In view of (3.12) the following question arises.

QUESTION 3.5. *Is it possible to specify the density function of CVT* $\{\Omega_i, i = 1, 2, \ldots, k\}$ *and its generator points in order to minimize the functional*

$$F_E = \sum_{i=1}^{k} L_{\Omega_i}(\nabla f) \int_{\Omega_i} \|\boldsymbol{x} - \boldsymbol{c}_{\Omega_i}\|^2 d\boldsymbol{x}?$$

To answer this question for the class of twice continuously differentiable functions we first prove the following lemma.

LEMMA 3.6. *Let $f$ be a twice continuously differentiable function, let $H_f$ be its Hessian matrix, and let $\|H_f\|$ be the second norm (modulus of the maximum eigenvalue) of the Hessian matrix. Then for any point $\boldsymbol{x} \in \Omega_i$, $L_{\Omega_i}(\nabla f) \leq \|H_f\|(\boldsymbol{x})$, $i = 1, 2, \ldots, k$.*

*Proof.* Assume that, contrary to the statement of the lemma, there exists at least one point $\boldsymbol{z} \in \Omega_i$ such that $L_{\Omega_i}(\nabla f) > \|H_f\|(\boldsymbol{z})$. Thus, there exists the constant $M > 0$ such that

$$\|H_f\|(\boldsymbol{z}) < M < L_{\Omega_i}(\nabla f). \tag{3.14}$$

Now we take $\boldsymbol{\xi}, \boldsymbol{\eta} \in \Omega_i$ to be certain points and consider the function $h_{\boldsymbol{a}}(t)$ of the variable $t \in [0, 1] \subset \mathbb{R}$ with constant vector $\boldsymbol{a}$:

$$h_{\boldsymbol{a}}(t) = \langle \boldsymbol{a}, \nabla f(\boldsymbol{\eta} + t(\boldsymbol{\xi} - \boldsymbol{\eta})) \rangle.$$

Then we have

$$\langle \boldsymbol{a}, \nabla f(\boldsymbol{\xi}) - \nabla f(\boldsymbol{\eta}) \rangle = \frac{h_{\boldsymbol{a}}(1) - h_{\boldsymbol{a}}(0)}{1 - 0}.$$

Under the conditions of the mean value theorem there exists a point $t_{\boldsymbol{a}} \in (0, 1)$ such that

$$\begin{aligned} \langle \boldsymbol{a}, \nabla f(\boldsymbol{\xi}) - \nabla f(\boldsymbol{\eta}) \rangle = h'(t_{\boldsymbol{a}}) &= \langle \boldsymbol{a}, H_f(\boldsymbol{\eta} + t_{\boldsymbol{a}}(\boldsymbol{\xi} - \boldsymbol{\eta})) \cdot (\boldsymbol{\xi} - \boldsymbol{\eta}) \rangle \\ &= \langle \boldsymbol{a}, H_f(\boldsymbol{\zeta}_{\boldsymbol{a}}) \cdot (\boldsymbol{\xi} - \boldsymbol{\eta}) \rangle, \end{aligned}$$

where the dot means multiplication of matrix by vector. Let us choose the points $\boldsymbol{\xi}, \boldsymbol{\eta} \in \Omega_i$ in such a way that $\zeta_{\boldsymbol{a}} = \boldsymbol{\eta} + t_{\boldsymbol{a}}(\boldsymbol{\xi} - \boldsymbol{\eta}) = \boldsymbol{z}$.

Now taking the supremum norm for all $\|\boldsymbol{a}\| = 1$ and using the Cauchy–Schwarz inequality, one has

$$\|\nabla f(\boldsymbol{\xi}) - \nabla f(\boldsymbol{\eta})\| \le \sup_{\|\boldsymbol{a}\|=1} \langle\, \boldsymbol{a}, H_f(\boldsymbol{z}) \cdot (\boldsymbol{\xi} - \boldsymbol{\eta})\rangle < M\|\boldsymbol{\xi} - \boldsymbol{\eta}\|. \tag{3.15}$$

The first inequality in (3.15) is obtained by choosing $\boldsymbol{a} = \frac{\nabla f(\boldsymbol{\xi}) - \nabla f(\boldsymbol{\eta})}{\|\nabla f(\boldsymbol{\xi}) - \nabla f(\boldsymbol{\eta})\|}$ in the inner product $\langle\, \boldsymbol{a}, \nabla f(\boldsymbol{\xi}) - \nabla f(\boldsymbol{\eta})\rangle$; the second one follows from the left inequality of (3.14). Since $L_{\Omega_i}(\nabla f)$ is the smallest possible constant such that, for all $\boldsymbol{\xi}, \boldsymbol{\eta} \in \Omega_i$,

$$\|\nabla f(\boldsymbol{\xi}) - \nabla f(\boldsymbol{\eta})\| \le L_{\Omega_i}(\nabla f)\|\boldsymbol{\xi} - \boldsymbol{\eta}\|,$$

then from (3.15) one has $L_{\Omega_i}(\nabla f) \le M$. This is in contradiction to the right inequality of (3.14), which proves the statement of the lemma. ∎

Now we are in a position to write the global error estimate for our cubature formulas and describe the way of minimizing it.

THEOREM 3.7. *Let $f(\boldsymbol{x})$ be a twice continuously differentiable function with Hessian matrix $H_f$ and $\mu(\boldsymbol{x}) = \|H_f\|(\boldsymbol{x}) + 1$; then the estimate of the energy functional is as follows:*

$$\begin{aligned} F_E &= \sum_{i=1}^{k} L_{\Omega_i}(\nabla f) \int_{\Omega_i} \|\boldsymbol{x} - \boldsymbol{c}_i\|^2 \, d\boldsymbol{x} \\ &\le \left(1 + 3 \max_{i=1,\dots,k} \overline{\mu}_i\right) \sum_{i=1}^{k} \int_{\Omega_i} \mu(\boldsymbol{x}) \, \|\boldsymbol{x} - \boldsymbol{x}_i\|^2 \, d\boldsymbol{x}, \end{aligned} \tag{3.16}$$

*where $\boldsymbol{x}_i$, $i = 1, \dots, k$, are generator points of CVT $\Omega_i$,*

$$\boldsymbol{c}_i = \boldsymbol{c}_{\Omega_i} = \frac{\int_{\Omega_i} \boldsymbol{x} \, d\boldsymbol{x}}{V_n(\Omega_i)}, \quad \overline{\mu}_i = \frac{\int_{\Omega_i} \mu(\boldsymbol{x}) \, d\boldsymbol{x}}{V_n(\Omega_i)}.$$

*The right-hand side of* (3.16) *can be minimized if we take*

$$\boldsymbol{x}_i = \boldsymbol{s}_{\Omega_i} = \frac{\int_{\Omega_i} \mu(\boldsymbol{x}) \boldsymbol{x} \, d\boldsymbol{x}}{\int_{\Omega_i} \mu(\boldsymbol{x}) \, d\boldsymbol{x}}.$$

*Proof.* Using Lemma 3.6 and the triangle inequality, we can write for $F_E$ the estimate

$$\begin{aligned} F_E &\le \sum_{i=1}^{k} \int_{\Omega_i} \mu(\boldsymbol{x}) \, \|\boldsymbol{x} - \boldsymbol{c}_i\|^2 \, d\boldsymbol{x} \\ &\le \sum_{i=1}^{k} \int_{\Omega_i} \mu(\boldsymbol{x}) \{\|\boldsymbol{x} - \boldsymbol{x}_i\|^2 + 2\|\boldsymbol{x} - \boldsymbol{x}_i\|\|\boldsymbol{c}_i - \boldsymbol{x}_i\| + \|\boldsymbol{c}_i - \boldsymbol{x}_i\|^2\} d\boldsymbol{x}. \end{aligned} \tag{3.17}$$

Note that both of the functions $\|\boldsymbol{x} - \boldsymbol{x}_i\|$ and $\|\boldsymbol{x} - \boldsymbol{x}_i\|^2$ are convex; then using (2.14) one has

$$V_n(\Omega_i)\|\boldsymbol{c}_i - \boldsymbol{x}_i\| \le \int_{\Omega_i} \|\boldsymbol{x} - \boldsymbol{x}_i\| d\boldsymbol{x}, \quad V_n(\Omega_i)\|\boldsymbol{c}_i - \boldsymbol{x}_i\|^2 \le \int_{\Omega_i} \|\boldsymbol{x} - \boldsymbol{x}_i\|^2 d\boldsymbol{x}.$$

Applying these inequalities, from (3.17) we have

$$F_E \le \sum_{i=1}^{k} \int_{\Omega_i} \mu(\boldsymbol{x}) \|\boldsymbol{x}-\boldsymbol{x}_i\|^2 d\boldsymbol{x} + \frac{2}{V_n(\Omega_i)} \int_{\Omega_i} \mu(\boldsymbol{x}) \|\boldsymbol{x}-\boldsymbol{x}_i\| d\boldsymbol{x} \int_{\Omega_i} \|\boldsymbol{x}-\boldsymbol{x}_i\| d\boldsymbol{x} + \frac{1}{V_n(\Omega_i)} \int_{\Omega_i} \mu(\boldsymbol{x}) d\boldsymbol{x} \int_{\Omega_i} \|\boldsymbol{x}-\boldsymbol{x}_i\|^2 d\boldsymbol{x}.$$

Using this estimate together with the obvious fact that $\mu(\boldsymbol{x}) = \|H_f\|(\boldsymbol{x}) + 1 \ge 1$ gives

$$\begin{aligned} F_E \le & \sum_{i=1}^{k} \int_{\Omega_i} \mu(\boldsymbol{x}) \|\boldsymbol{x}-\boldsymbol{x}_i\|^2 d\boldsymbol{x} \\ & + \frac{2}{V_n(\Omega_i)} \int_{\Omega_i} \mu(\boldsymbol{x}) \|\boldsymbol{x}-\boldsymbol{x}_i\| d\boldsymbol{x} \int_{\Omega_i} \mu(\boldsymbol{x}) \|\boldsymbol{x}-\boldsymbol{x}_i\| d\boldsymbol{x} \\ & + \frac{1}{V_n(\Omega_i)} \int_{\Omega_i} \mu(\boldsymbol{x}) d\boldsymbol{x} \int_{\Omega_i} \mu(\boldsymbol{x}) \|\boldsymbol{x}-\boldsymbol{x}_i\|^2 d\boldsymbol{x}. \end{aligned} \tag{3.18}$$

The Cauchy–Schwarz inequality for integral scalar products gives

$$\begin{aligned} \left( \int_{\Omega_i} \mu(\boldsymbol{x}) \|\boldsymbol{x}-\boldsymbol{x}_i\| d\boldsymbol{x} \right)^2 &\le \left( \int_{\Omega_i} \sqrt{\mu(\boldsymbol{x})} (\sqrt{\mu(\boldsymbol{x})} \|\boldsymbol{x}-\boldsymbol{x}_i\|) d\boldsymbol{x} \right)^2 \\ &\le \int_{\Omega_i} \mu(\boldsymbol{x}) d\boldsymbol{x} \int_{\Omega_i} \mu(\boldsymbol{x}) \|\boldsymbol{x}-\boldsymbol{x}_i\|^2 d\boldsymbol{x}. \end{aligned}$$

Applying this inequality to the second term in (3.18), we finally obtain

$$F_E \le \sum_{i=1}^{k} (1 + 3\overline{\mu}_i) \int_{\Omega_i} \mu(\boldsymbol{x}) \|\boldsymbol{x}-\boldsymbol{x}_i\|^2 d\boldsymbol{x}.$$

Now the desired estimate (3.16) follows by taking the maximum of $\overline{\mu}_i$ over all Voronoi cells.

In the end of the proof we should underline that the point of the local minimum of functional $\sum_{i=1}^{k} \int_{\Omega_i} \mu(\boldsymbol{x}) \|\boldsymbol{x}-\boldsymbol{x}_i\|^2 d\boldsymbol{x}$ can be found by equaling its gradient (as a function of $\boldsymbol{x}_i$) to zero:

$$2 \sum_{i=1}^{m} \int_{\Omega_i} \mu(\boldsymbol{x}) (\boldsymbol{x}-\boldsymbol{x}_i) d\boldsymbol{x} = 0,$$

from which it follows that the point of local minimum is

$$\boldsymbol{x}_i = \boldsymbol{s}_{\Omega_i} = \frac{\int_{\Omega_i} \mu(\boldsymbol{x}) \boldsymbol{x}\, d\boldsymbol{x}}{\int_{\Omega_i} \mu(\boldsymbol{x})\, d\boldsymbol{x}}. \tag{3.19}$$

∎

Theorem 3.7 gives the constructive way for building cubature formulas with the best global error estimates. To this end one should construct CVTs with density equal to the second norm of Hessian of integrand plus one and then apply the formulas $Q_\Omega^{\mathrm{tra}}$, $Q_\Omega^{\mathrm{mid}}$, $Q_\Omega^{\mathrm{Ha}}$, or $Q_\Omega^{\mathrm{Si}}$. In any case the most accurate formulas are going to be the $Q_\Omega^{\mathrm{Ha}}$ with second order of approximation and the formula $Q_\Omega^{\mathrm{Si}}$ of higher order. Let us check this conclusion and other results of the paper in numerical tests.

**4. Numerical tests.** In this section we provide some numerical tests, which we perform in order to validate our theoretical predictions and to compare the set of cubature formulas described in the previous sections. Here, for the sake of brevity, we did not perform a numerical comparison with the classical cubature formulas, which have the same order of approximation and use the values of the integrand at certain points. However, it is shown in [4] that these latter give the worst results compared to a class of extended cubature formulas developed there.

We shall first consider the following two bivariate functions:

$$f_1(\boldsymbol{x}) = \exp(ax + by),\ a, b \in \mathbb{R}, \tag{4.1}$$

$$f_2(\boldsymbol{x}) = y \arctan(a(x + y)),\ a \in \mathbb{R}^+, \tag{4.2}$$

where $\boldsymbol{x} = (x, y) \in \mathbb{R}^2$. Both of them are infinitely differentiable functions having singularities (large gradients), when $a$ and $b$ are large enough. Note that $f_1(x, y)$ is componentwise convex and $f_2(x, y)$ is not convex; see Figure 4.1.

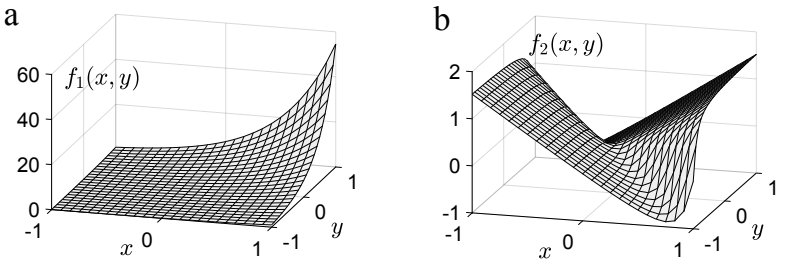


FIG. 4.1. *Test functions:* (a) $f_1(x, y)$ *for the case* $a = b = 2$, *and* (b) $f_2(x, y)$ *for* $a = 10$.

The second norm of the Hessian matrix for the function $f_1(\boldsymbol{x})$ is

$$\mu_1(\boldsymbol{x}) = (a^2 + b^2) f_1(\boldsymbol{x}) = (a^2 + b^2) \exp(ax + by). \tag{4.3}$$

The second norm of the Hessian matrix for the function $f_2(\boldsymbol{x})$ is

$$\mu_2(\boldsymbol{x}) = \frac{a\sqrt{3 + a^2(6x^2 + 4v_3 - 2y^2) + a^4 v_1^2(3v_2 - 2v_3) + 2\sqrt{2}v_4}}{(1 + a^2 v_1^2)^2}, \tag{4.4}$$

where

$$v_1 = x + y, \quad v_2 = x^2 + y^2, \quad v_3 = xy, \quad v_4 = |1 + a^2(x^2 - y^2)|\sqrt{1 + 2a^2 x v_1 + a^4 v_1^2 v_2}.$$

We shall first test our cubature formulas for $f_1(x, y)$ and $f_2(x, y)$ in the simple square domain $(x, y) \in P = [-1, 1]^2$ after constructing its CVT with uniform and nonuniform density for different values of $a$ and $b$. Then we shall proceed with integrating another function over a more complex domain formed by two semicircles having a unique center. For constructing a CVT we use PolyMesher: a general-purpose mesh generator for polygonal elements written in MATLAB by Cameron Talischi, Glaucio H. Paulino, Anderson Pereira, and Ivan F. M. Menezes; see [16]. This program package uses a sign distance function for determining the domain, reflections of generator points for linear approximation of its boundary, and Lloyd's algorithm

for constructing CVTs. We modified some parts of the code given in [16] for taking into account nonuniform density of Voronoi cells. The main modifications were the following:

- Function "PolyMshr_CntrdPly" was changed in order to compute the coordinates of the generator point of each cell in the case of nonuniform density, as in (3.19). In this formula for computing the integrals of $\mu(\boldsymbol{x})$ over $\Omega_i$ we used our bivariate version of the Simpson rule $Q_{\Omega}^{\mathrm{Si}}(\mu)$. The input parameters for using this rule were the function $\mu(\boldsymbol{x}) \in \{\mu_1, \mu_2\}$; the coordinates of point $\boldsymbol{c}_{\Omega_i}$ (see (2.1)) and the volume $V_2(\Omega_i)$ computed by PolyMesher; the integral of $\mu(\boldsymbol{x})$ over the facets of each $\Omega_i$ and the distances from $\boldsymbol{c}_{\Omega_i}$ to these facets. For $f_1(\boldsymbol{x})$ we succeed in getting analytic expressions for integrals over facets, and for function $f_2(\boldsymbol{x})$ they were computed by the classical Simpson rule.
- To avoid the emergence of elongated cells that appeared while constructing CVTs with nonuniform density for cases with the most steep gradients in the iterations of Lloyd's algorithm, we check that the distances from the point $\boldsymbol{c}_{\Omega_i}$ to all of the facets of $\Omega_i$ do not differ significantly, and check the same for the distances to all of the vertices. Usually the requirement that the relations of these distances are less than 3–4 was used. If this requirement holds for current $\Omega_i$, we move its generator point in accordance with Lloyd's algorithm; if not, then the generator point remained fixed at the current iteration.
- The parameter $c$ of function "PolyMesher" was changed to 100, and the function "PolyMshr_Rflct" was modified in order to exclude the reflected cells lying outside the domain $P$.
- The algorithm of computation of the "nondimensional" error parameter $E_r$ serving to stop the iterations was changed. The stopping criteria for Lloyd's method was set as $E_r < 10^{-4}$.

The resulting views of CVTs for square domains generated using density functions (4.3), (4.4) are shown in Figure 4.2.

Below we compare the results of the algorithm with constant density (ACD) and of the algorithm with nonconstant density (ANCD).

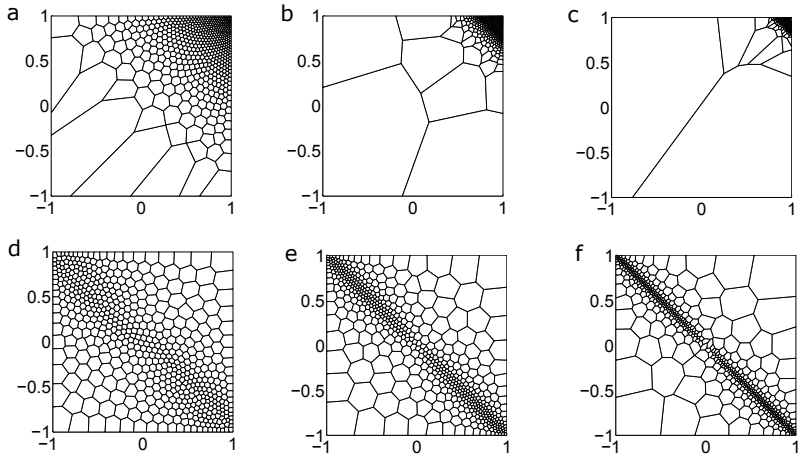


FIG. 4.2. *Centroidal Voronoi tessellations of square domains obtained with density function* $\mu_1(\boldsymbol{x})$ *as* (a) $a = b = 6$, (b) $a = b = 21$, (c) $a = b = 51$*; and with density function* $\mu_2(\boldsymbol{x})$ *as* (d) $a = 6$, (e) $a = 21$, (f) $a = 51$. *Number of cells is* $24^2$.

**4.1. Integration of convex exponential function over square domain.** We shall use the proposed methods $Q_\Omega^{\rm tra}(f)$, $Q_\Omega^{\rm mid}(f)$, $Q_\Omega^{\rm Ha}(f)$, $Q_\Omega^{\rm Si}(f)$ for computing numerical values of the integrals of $f(\boldsymbol{x}) = f_1(x,y)$ or $f(\boldsymbol{x}) = f_2(x,y)$ over the square $P = [-1,1]^2 \subset \mathbb{R}^2$ . To this end we use CVTs generated by the original PolyMesher (for uniform density of cells) and by our modification of it (for nonuniform density of cells). In what follows, $N$ is the square root of the number of Voronoi cells (approximate mean number of cells along one axis in two dimensions); $\Omega_i$ is the cell of Voronoi tessellation of $P$, $i = 1, \ldots, N^2$. Numerical values of integrals of $f_1(\boldsymbol{x})$, $f_2(\boldsymbol{x})$ over $P$ will be computed by applying our approximate integral formulas in each of the cells $\Omega_i$ and by summing the results over all $i = 1, \ldots, N^2$. We shall denote such summary expressions by $Q_N^{\rm tra}(f)$, $Q_N^{\rm mid}(f)$, $Q_N^{\rm Ha}(f)$, $Q_N^{\rm Si}(f)$ correspondingly.

The exact values of integrals of $f_1(\boldsymbol{x})$ and $f_2(\boldsymbol{x})$ over $P$ are as follows:

$$I(f_1) = \frac{4\sinh(a)\sinh(b)}{ab},$$

$$I(f_2) = -\frac{8a^2 - 2a(3+4a^2)\arctan(2a) + \log(1+4a^2)}{6a^3}.$$

Let $E_N^{\rm tra}(f)$ be the relative error of method $Q_N^{\rm tra}(f)$, obtained using CVTs:

$$E_N^{\rm tra}(f) = \frac{Q_N^{\rm tra}(f) - I(f)}{I(f)},\ f \in \{f_1, f_2\}. \tag{4.5}$$

By analogy the relative errors $E_N^{\rm mid}(f)$, $E_N^{\rm Ha}(f)$, and $E_N^{\rm Si}(f)$ can be defined for others of the proposed methods.

In Figure 4.3 common logarithms of the moduli of relative errors for the case $f = f_1(\boldsymbol{x})$, $a = b = 1$ are represented both for constant density function (graphs a and c) and for density function $\mu_1(\boldsymbol{x})$ (graphs b and d). For both ACD and ANCD the least accurate are formulas $Q_N^{\rm tra}(f_1)$ and $Q_N^{\rm mid}(f_1)$; the moduli of their errors are very close. Comparatively good results can be obtained by using the formula $Q_N^{\rm Ha}(f_1)$; its error is less than that for the trapezoidal and midpoint ones in 3 times approximately; see also (3.9)–(3.11). The Simpson rule $Q_N^{\rm Si}(f_1)$ shows the best results. The quantitative data, characterizing the accuracy of these formulas for other values of $a$ and $b$, is given in Tables 4.1 and 4.2.

It is worth noting that for small $a$ and $b$ ACD and ANCD give very close results. A careful consideration of graphs of errors in Figure 4.3 enables us to see only a small advantage in accuracy of ANCD for the fourth order method, which is not larger than two times. More detailed information is given in the last row of Table 4.1.

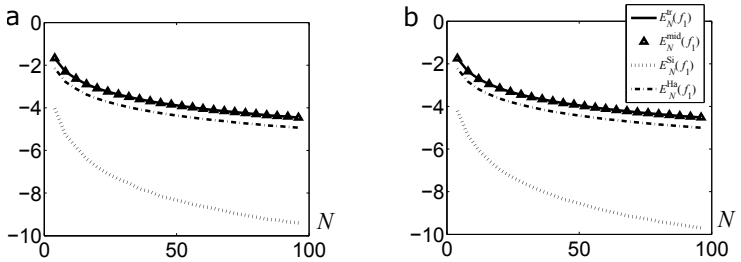


FIG. 4.3. *Common logarithms of the moduli of relative errors obtained while integrating* $f_1(\boldsymbol{x})$ *with* $a = b = 1$ *using CVT with uniform density* (a) *and using concentrated CVT* (b).

TABLE 4.1
*Errors of integration obtained in tests for $f_1(\boldsymbol{x})$ with $a = b = 1$.*

| $N$ | $E_N^{\mathrm{tra}}(f_1)$ | | $E_N^{\mathrm{mid}}(f_1)$ | | $E_N^{\mathrm{Ha}}(f_1)$ | | $E_N^{\mathrm{Si}}(f_1)$ | |
|---|---|---|---|---|---|---|---|---|
| | ACD | ANCD | ACD | ANCD | ACD | ANCD | ACD | ANCD |
| 4 | -2.12E-02 | -1.79E-02 | 2.1E-02 | 1.77E-02 | -7.13E-03 | -6E-03 | -6.19E-05 | -4.07E-05 |
| 8 | -5E-03 | -4.38E-03 | 4.98E-03 | 4.37E-03 | -1.67E-03 | -1.46E-03 | -3.67E-06 | -2.86E-06 |
| 16 | -1.26E-03 | -1.11E-03 | 1.26E-03 | 1.11E-03 | -4.2E-04 | -3.71E-04 | -2.69E-07 | -1.9E-07 |
| 32 | -3.19E-04 | -2.71E-04 | 3.19E-04 | 2.71E-04 | -1.06E-04 | -9.04E-05 | -2E-08 | -1.15E-08 |
| 64 | -7.91E-05 | -6.79E-05 | 7.91E-05 | 6.79E-05 | -2.64E-05 | -2.26E-05 | -1.27E-09 | -7.20E-10 |
| 128 | -1.96E-05 | -1.7E-05 | 1.96E-05 | 1.7E-05 | -6.55E-06 | -5.66E-06 | -1.03E-10 | -4.43E-11 |
| 256 | — | -4.95E-06 | 4.94E-06 | 4.95E-06 | — | -1.65E-06 | — | -4.27E-12 |
| $C_{err}$ | **2.9941** | 2.996 | **2.9882** | 2.9919 | **1** | 1 | | |
| $C_{err2}$ | 1.1594 | | 1.1359 | | 1.1599 | | 1.6757 | |

TABLE 4.2
*Orders of convergence obtained in tests for $f_1(\boldsymbol{x})$ with $a = b = 1$.*

| $N$ | $E_N^{\mathrm{tra}}(f_1)$ | | $E_N^{\mathrm{mid}}(f_1)$ | | $E_N^{\mathrm{Ha}}(f_1)$ | | $E_N^{\mathrm{Si}}(f_1)$ | |
|---|---|---|---|---|---|---|---|---|
| | ACD | ANCD | ACD | ANCD | ACD | ANCD | ACD | ANCD |
| 8 | 2.0853 | 2.0278 | 2.0758 | 2.0207 | 2.0947 | 2.0348 | 4.0761 | 3.8306 |
| 16 | 1.9898 | 1.978 | 1.9875 | 1.976 | 1.992 | 1.9801 | 3.7684 | 3.9114 |
| 32 | 1.9775 | 2.0365 | 1.9769 | 2.0359 | 1.9782 | 2.037 | 3.7519 | 4.0457 |
| 64 | 2.0138 | 1.9983 | 2.0136 | 1.9982 | 2.0141 | 1.9985 | 3.9775 | 3.9997 |
| 128 | 2.0098 | 1.9992 | 2.0097 | 1.9991 | 2.0098 | 1.9992 | 3.6172 | 4.0221 |
| 256 | — | 1.7780 | 1.9912 | 1.778 | — | 1.778 | — | 3.3752 |
| aver | 2.0152 | 1.9696 | 2.0091 | 1.968 | 2.0178 | 1.9713 | 3.8382 | 3.8641 |

In Figure 4.4 the moduli of relative errors of integration of $f_1(\boldsymbol{x})$ are shown in $\log_{10}$ scale for $a = 10$ and $b = 50$. Here the difference between ACD and ANCD is much more obvious. The advantage in accuracy for second order methods is hundreds of times and for the fourth order method is about tens of thousands of times.

In Table 4.1 the relative errors obtained in tests for $f_1(\boldsymbol{x})$ with $a = b = 1$ are given. It is necessary to note that while computing the integral of convex function $f_1(\boldsymbol{x})$ by the formulas $Q_P^{\mathrm{tra}}(f_1)$, $Q_P^{\mathrm{mid}}(f_1)$ and $Q_P^{\mathrm{Ha}}(f_1)$ we had been checking the inequalities (2.9), (2.14), and (2.16), respectively. Numerical values of the integral often satisfied them.

In the penultimate row of Table 4.1 the values of relative constant factor of errors $C_{err}$ are given for methods $Q_P^{\mathrm{tra}}(f_1)$, $Q_P^{\mathrm{mid}}(f_1)$, and $Q_P^{\mathrm{Ha}}(f_1)$. All of these methods have the second order of convergence, but the values of its errors differ because of this constant factor. The values of $C_{err}$ were computed by averaging the result of division of this errors by $E_N^{\mathrm{Ha}}(f)$ for those intervals of $N$, where the experimental order of convergence (see Table 4.2) turns out to be close to the theoretical one, assuming that the error factor of $Q_\Omega^{\mathrm{Ha}}(f)$ is equal to 1. Note that these operations were done separately for the results obtained by ACD and ANCD. According to numerical tests, the moduli of errors of $Q_P^{\mathrm{tra}}(f_1)$ and $Q_P^{\mathrm{mid}}(f_1)$ cubature formulas coincide with high accuracy, and the constant factors of their errors are approximately three times larger than for $Q_P^{\mathrm{Ha}}(f_1)$ cubature formula.

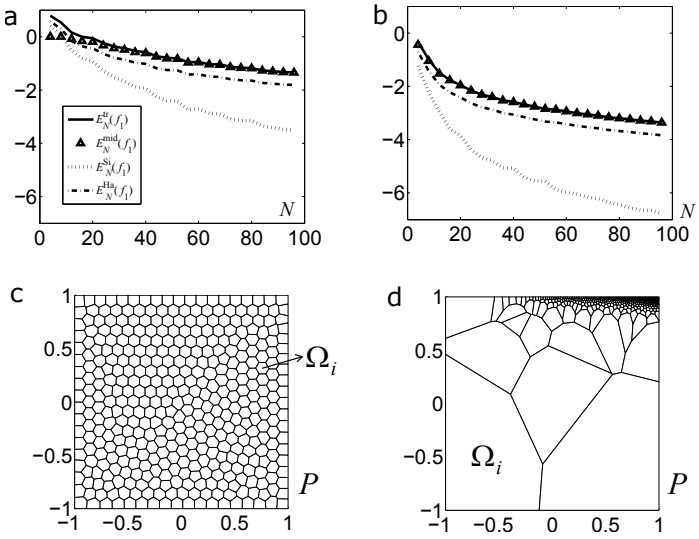


FIG. 4.4. *Common logarithms of the relative errors of integration of function $f_1$ with $a = 10$ and $b = 50$ obtained using CVT with uniform density* (a) *and using concentrated CVT* (b). *Views of the corresponding CVTs are given in panels* (c) *and* (d).

The last row of Table 4.1 contains the averaged moduli of the relations between errors obtained using ACD and ANCD. The value of $C_{err2}$ shows how many times the accuracy of integration using ANCD exceeds the accuracy of integration using ACD for the considered values of $a$ and $b$. As was mentioned before, for small $a$ and $b$ this advantage of ANCD is small.

In Table 4.2 the orders of convergence obtained in the same tests for $f_1(\boldsymbol{x})$ are given. To compute the order of convergence of method $Q_P^{\mathrm{tra}}(f_1)$ we used the formula

$$R_N^{\mathrm{tra}}(f_1) = \log_2 \frac{|Q_{P,N/2}^{\mathrm{tra}}(f_1) - I(f_1)|}{|Q_{P,N}^{\mathrm{tra}}(f_1) - I(f_1)|}, \tag{4.6}$$

where $Q_{P,N}^{\mathrm{tra}}(f_1)$ is the approximate value of integral of $f_1$, obtained using the trapezoidal rule $Q_P^{\mathrm{tra}}(f)$ and the Voronoi tessellation of $P$ with $N^2$ cells. Similar formulas were used to obtain the orders of convergence for others of the proposed rules $R_N^{\mathrm{mid}}(f_1)$, $R_N^{\mathrm{Ha}}(f_1)$, and $R_N^{\mathrm{Si}}(f_1)$. These formulas imply that we should increase step by step the value of $N$ by two times and compute the order staring from the second step. This method was implemented, and the data given in Table 4.2 was obtained. The last row of Table 4.2 contains average values of the order. It is easy to see that these numerical results correspond to theoretical orders with good accuracy (see Remark 2.8). We can also note that for rules $Q_P^{\mathrm{tra}}(f)$, $Q_P^{\mathrm{mid}}(f)$, and $Q_P^{\mathrm{Ha}}(f)$ the order of convergence of ANCD is a little less than that for ACD. This can be caused by the larger complexity of ANCD, but for arc-tangent functions the situation is the opposite.

**4.2. Integration of arc-tangent function over square domain.** The results of integration of $f_2(\boldsymbol{x})$ look similar to those for $f_1(\boldsymbol{x})$; see Figures 4.5 and 4.6. For moderate values of $a$ the advantage of ANCD is less than that for larger $a$. However, for the function $f_2(\boldsymbol{x})$ the specific oscillations of the errors appear.

When talking about oscillations of $E_N^{\mathrm{tra}}(f)$ and $E_N^{\mathrm{mid}}(f)$ for large $a$ (see Figure 4.6), the reason for these oscillations is that the convergence starts from large

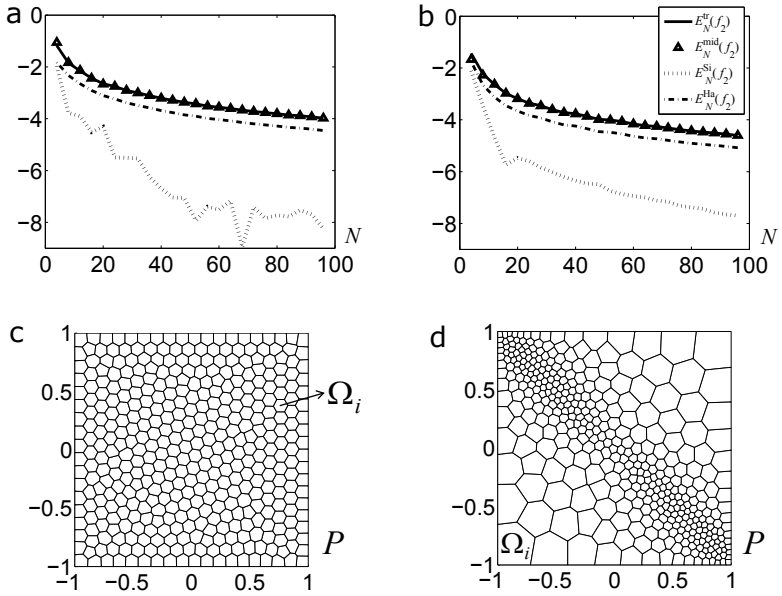


FIG. 4.5. *Common logarithms of the moduli of relative errors obtained while integrating* $f_2(\boldsymbol{x})$ *with* $a = 10$ *using CVT with uniform density* (a) *and using concentrated CVT* (b). *Views of the corresponding CVTs are given in panels* (c) *and* (d).

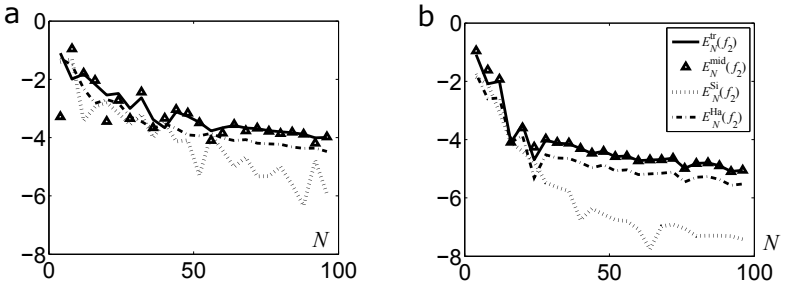


FIG. 4.6. *Common logarithms of the moduli of relative errors obtained while integrating* $f_2(\boldsymbol{x})$ *with* $a = 50$ *using CVT with uniform density* (a) *and using concentrated CVT* (b).

values of $N$. If $N$ is small, the tessellation appears not to be fine enough to resolve the singularity located in the vicinity of the line $y = -x$. The regular behavior of the errors appears when a sufficient number of cells fall into this vicinity. If using ACD with $a = 50$, the convergence of the trapezoidal and midpoint rules starts at $N = N_0 \approx 70$ (see Figure 4.6(a)), and if $N < N_0$, the error of midpoint rule demonstrates the most chaotic behavior since it uses some information about the integrand (only its value in one central point of each cell). Analogously, using ANCD with $a = 50$ for $N \geq N_0 \approx 30$, one can observe the convergence, but even for $N < N_0$ there are not so many oscillations of $E_N^{\mathrm{mid}}(f)$, which shows the better properties of stability of ANCD in general. It should be noted that in any case formula $E_N^{\mathrm{Ha}}(f)$ shows the best stability.

Thus, the important distinction between exponential and arc-tangent functions that effects the accuracy is that unlike the first one, the last one has the local singularity. The increase in the values of $a$ and $b$ of function $f_1(\boldsymbol{x})$ leads to a decrease in

TABLE 4.3
*Errors of integration obtained in tests for $f_2(\boldsymbol{x})$ with $a = 10$.*

| $N$ | $E_N^{\mathrm{tra}}(f_1)$ | | $E_N^{\mathrm{mid}}(f_1)$ | | $E_N^{\mathrm{Ha}}(f_1)$ | | $E_N^{\mathrm{Si}}(f_1)$ | |
|---|---|---|---|---|---|---|---|---|
| | ACD | ANCD | ACD | ANCD | ACD | ANCD | ACD | ANCD |
| 4 | -6.54E-02 | -3.65E-02 | 8.64E-02 | 2.12E-02 | -1.48E-02 | -1.73E-02 | 7E-03 | -5.11E-03 |
| 8 | -1.43E-02 | -5.96E-03 | 1.46E-02 | 5.26E-03 | -4.66E-03 | -2.22E-03 | 1.11E-04 | -2.33E-04 |
| 16 | -3.67E-03 | -1.05E-03 | 3.61E-03 | 1.04E-03 | -1.24E-03 | -3.51E-04 | -2.01E-05 | -1.23E-06 |
| 32 | -9.89E-04 | -2.48E-04 | 9.95E-04 | 2.46E-04 | -3.28E-04 | -8.33E-05 | 1.92E-06 | -6.3E-07 |
| 64 | -2.45E-04 | -6.03E-05 | 2.45E-04 | 6.01E-05 | -8.15E-05 | -2.02E-05 | 4.45E-08 | -6.65E-08 |
| 128 | -6.07E-05 | -1.42E-05 | 6.07E-05 | 1.42E-05 | -2.02E-05 | -4.74E-06 | 2.45E-09 | -4.28E-09 |
| 256 | -1.53E-05 | -3.43E-06 | 1.52E-05 | 3.43E-06 | -5.15E-06 | -1.14E-06 | -3.22E-08 | -3.79E-10 |
| $C_{err}$ | **2.9905** | 2.9906 | **2.9809** | 2.9813 | **1** | 1 | | |
| $C_{err2}$ | 3.4981 | | 3.8804 | | 3.321 | | 15.3388 | |

the convergence rate, whereas the increase in the values of $a$ of function $f_2(\boldsymbol{x})$ leads to growth of the number $N_0$ at which the convergence starts.

When talking about oscillations of $E_N^{\mathrm{Si}}(f)$ in tests with concentrated CVT (see Figures 4.5(b) and 4.6(b)), these oscillations are caused by the presence of a strong singularity of derivatives of $f_2(\boldsymbol{x})$ in a complex plain when $a$ is large. This singularity leads to a very rapid growth of high order derivatives of the function, which is a problem for methods of high order. In tests with an exponential function, the behavior of the derivatives of any order coincides with that of the function itself. The behavior of the derivatives of function $f_2(\boldsymbol{x})$ is completely different. The larger $a$ is, the greater the gap between the speed of growth of its second order and higher order derivatives, and the higher the amplitude of oscillations of the error (see also Figure 4.11). Our tests showed that for $a$ large enough this cannot be fixed by using the described concentration of Voronoi cells, since this concentration is constructed using the values of second order derivatives (not the higher order).

In Tables 4.3 and 4.4 the relative errors and the orders of convergence obtained in tests for $f_2(\boldsymbol{x})$ with $a = 10$ are given. All the data was computed as in section 4.1. The interesting fact is that although the function $f_2(\boldsymbol{x})$ is not convex, inequalities (2.9), (2.14), and (2.16) for it are satisfied. This remains true for not large values of $a$. If we increase the value of $a$ starting from 1, the first failure of inequality (2.14) by $Q_P^{\mathrm{mid}}(f_2)$ is observed for $a \approx 15$ and failure of (2.9) by $Q_P^{\mathrm{tra}}(f_2)$ is observed for $a \approx 30$. In any case $Q_\Omega^{\mathrm{Si}}(f_2)$ based on formula (2.20) again showed the extra rate convergence.

**4.3. Studding of correlations between the strength of singularities and the values of errors.** Comparing Figures 4.3, 4.4 and 4.5, 4.6, it is easy to note that usually (but not often) the larger the value of $a$ or $b$, the higher the value of the error. However, this dependence is not linear and is strongly correlated with the integrand's type of singularity and the order of integration formula. To get more details, let us observe the dependencies of the error on two parameters. The first is the parameter of singularity of the integrand, and the second is $N$. The rules of second order demonstrate similar behavior of the error; therefore we shall restrict our attention to the results for method $Q_N^{\mathrm{tra}}$ or $Q_N^{\mathrm{mid}}$ and compare them with the graphs of the error of method $Q_N^{\mathrm{Si}}$.

The tests for exponential functions with uniform density show nonlinear growth of the error with the diminishing rate, while increasing the value of $a = b$ (see Fig-

TABLE 4.4
*Orders of convergence obtained in tests for $f_2(\boldsymbol{x})$ with $a = 10$.*

| $N$ | $E_N^{\mathrm{tra}}(f_1)$ | | $E_N^{\mathrm{mid}}(f_1)$ | | $E_N^{\mathrm{Ha}}(f_1)$ | | $E_N^{\mathrm{Si}}(f_1)$ | |
|---|---|---|---|---|---|---|---|---|
| | ACD | ANCD | ACD | ANCD | ACD | ANCD | ACD | ANCD |
| 8 | 2.1938 | 2.6142 | 2.5621 | 2.0079 | 1.6697 | 2.9603 | 5.9809 | 4.4544 |
| 16 | 1.9623 | 2.5073 | 2.0194 | 2.3323 | 1.9049 | 2.6623 | 2.4608 | 7.5669 |
| 32 | 1.8913 | 2.0792 | 1.859 | 2.0851 | 1.9233 | 2.0733 | 3.3871 | 0.9658 |
| 64 | 2.0151 | 2.0396 | 2.0227 | 2.0334 | 2.0075 | 2.0458 | 5.4343 | 3.2417 |
| 128 | 2.0119 | 2.0872 | 2.0125 | 2.0837 | 2.0113 | 2.0907 | 4.1818 | 3.9593 |
| 256 | 1.9837 | 2.0483 | 1.993 | 2.0475 | 1.9745 | 2.0492 | 3.7152 | 3.4956 |
| aver | 2.0097 | 2.2293 | 2.0781 | 2.0983 | 1.9152 | 2.3136 | 2.955 | 3.9473 |

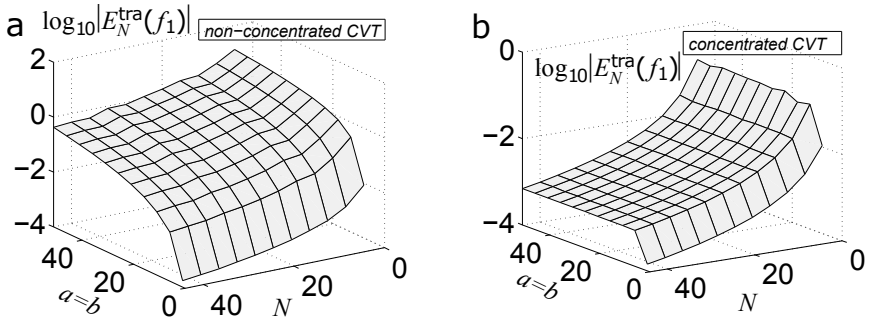


FIG. 4.7. *Dependence of the* $\log_{10}|E_N^{\mathrm{tra}}(f_1)|$ *on the values of* $a = b$ *and* $N$ *obtained using CVT with uniform density* (a) *and using concentrated CVT* (b).

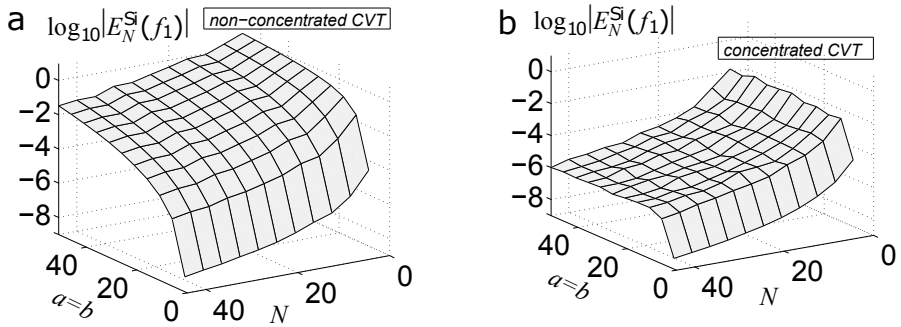


FIG. 4.8. *Dependence of the* $\log_{10}|E_N^{\mathrm{Si}}(f_1)|$ *on the values of* $a = b$ *and* $N$ *obtained using CVT with uniform density* (a) *and using concentrated CVT* (b).

ures 4.7(a) and 4.8(a)). This growth of $E_N^{\mathrm{Si}}(f_1)$ is faster than that of $E_N^{\mathrm{tra}}(f_1)$. In the case of concentrated Voronoi cells the error of integration of the exponential function has very rapid growth while increasing the values of $a$ and $b$ in the vicinity of zero. However, after exceeding a certain threshold value of $a = b \approx 5$ the errors reach a plateau and practically stay the same while further increasing $a$ and $b$; see Figures 4.7(b) and 4.8(b). We have checked that the growth of the errors for small $a$ and $b$ is not a jump discontinuity. To this end we test our methods on the shortened interval $a = b \in [0.5, 5]$ and see that all the graphs of the errors are smooth (see Figure 4.9).

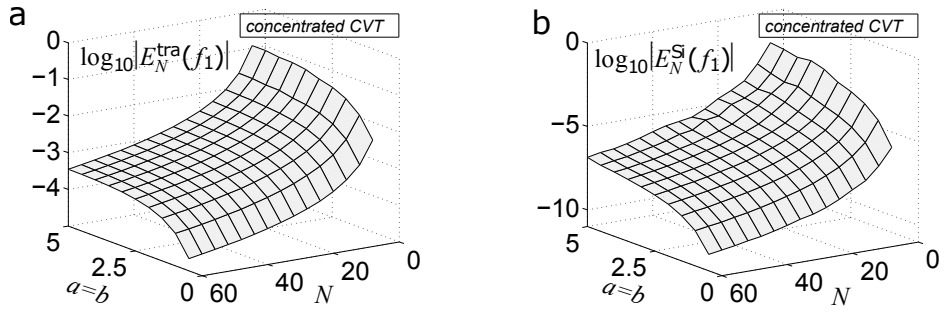


FIG. 4.9. *Dependence of the* $|\log_{10} E_N^{\mathrm{tra}}(f_1)|$ (a) *and* $\log_{10} E_N^{\mathrm{Si}}(f_1)$ (b) *on the values of* $a = b$ *and* $N$ *(*$a = b$ *are varied on the shortened interval).*

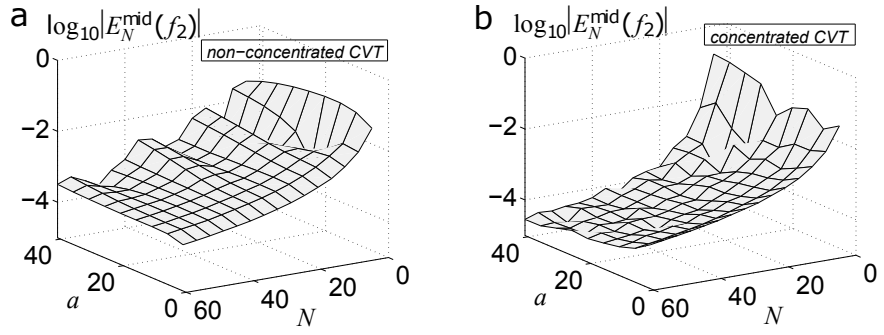


FIG. 4.10. *Dependence of the* $\log_{10}|E_N^{\mathrm{mid}}(f_2)|$ *on the values of* $a$ *and* $N$ *obtained using CVT with uniform density* (a) *and using concentrated CVT* (b).

We should mention here the interesting and surprising fact that $\log_{10}|E_N^{\mathrm{mid}}(f_2)|$ obtained using uniform tessellation does not change significantly on the average while increasing $a$, but it acquire large oscillations (see Figure 4.10(a)). This is caused by the oddness of arc-tangent function standing in $f_2(x)$. Indeed, the integration over the interval $[-l, l]$ of the odd function is zero, and therefore the contribution of the integral of $f_2(\boldsymbol{x})$ over the small vicinity of line $y = -x$ to the value of $I(f_2)$ is small, and the numerical methods also satisfy this property for any $N$. However, the absence of symmetry of tessellations with respect to the line $y = -x$ leads for large $a$ to loss of stability and to the oscillations that can be observed in Figure 4.10(a). As mentioned before, applying ANCD gives better stability, and it enables one to decrease the approximate values of the integral of $f_2(\boldsymbol{x})$ over the small vicinity of line $y = -x$ to its zero values, which minimizes the amplitude of oscillations (see Figure 4.10(b)).

Another important outcome from our tests is that the singularity gives opportunity for increasing of accuracy if using ANCD (see graph Figure 4.10(b)). Indeed, the increase of $a$ affects the singularity of function $f_2(\boldsymbol{x})$ and enables ANCD to recognize it while concentrating Voronoi cells; this leads to a decrease in the error, while increasing $a$. As a consequence, the value of the error of the Simpson rule also reduces if using ANCD instead of ACD (see Figure 4.11), but as was mentioned before, its oscillations cannot be eliminated.

It is also interesting to study how our methods react to growing the integrand's gradients with respect to each coordinate. To this end we fix $N = 30$ and consider the dependencies of the relative errors of integration of $f_1(\boldsymbol{x})$ on the values of $a$ and

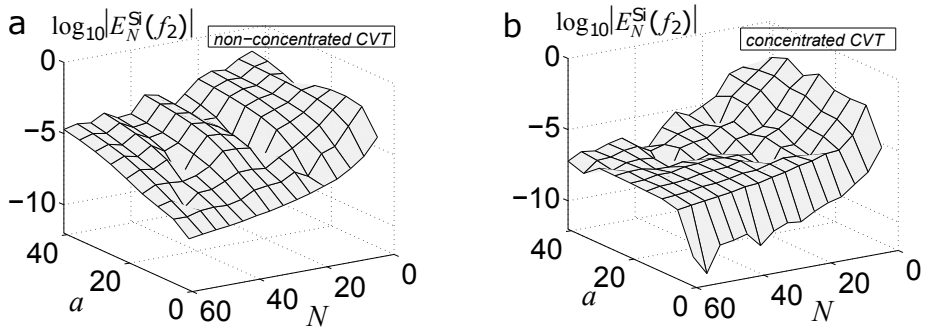


FIG. 4.11. *Dependence of the* $|\log_{10} E_N^{\mathrm{Si}}(f_2)|$ *on the values of* $a$ *and* $N$ *obtained using CVT with uniform density* (a) *and using concentrated CVT* (b).

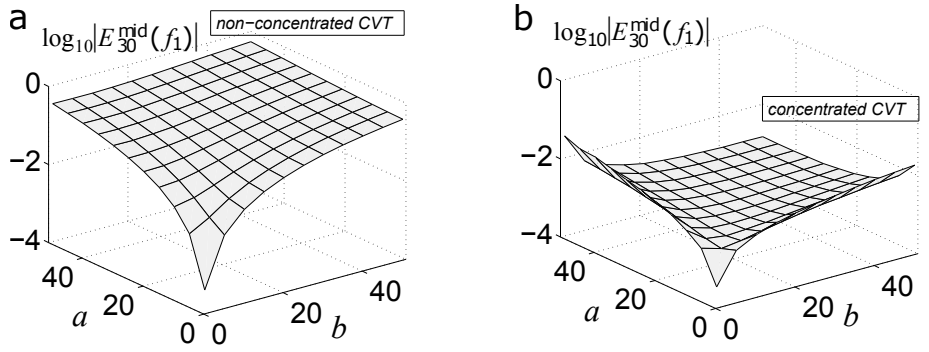


FIG. 4.12. *Dependence of the* $|\log_{10} E_{30}^{\mathrm{mid}}(f_1)|$ *on the values of* $a$ *and* $b$ *obtained using CVT with uniform density* (a) *and using concentrated CVT* (b).

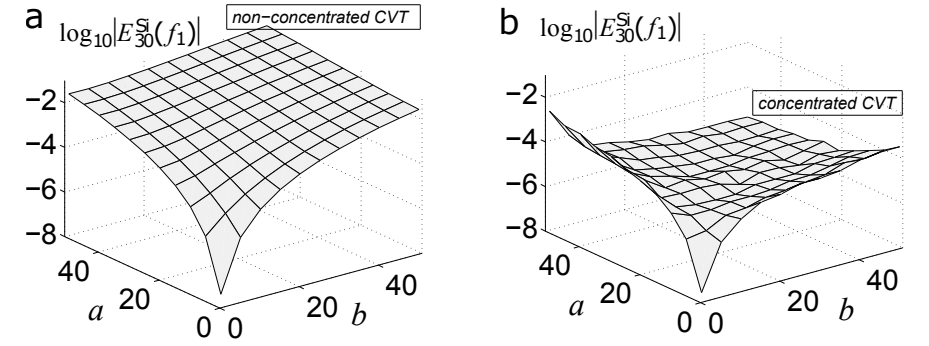


FIG. 4.13. *Dependence of the* $|\log_{10} E_{30}^{\mathrm{Si}}(f_1)|$ *on the values of* $a$ *and* $b$ *obtained for CVT with uniform density* (a) *and using concentrated CVT* (b).

$b$ separately (see Figures 4.12 and 4.13). It is natural that for tests with uniform density the errors grow with increases in $a$ and $b$. This growth is invariant with respect to permutation of $a$ and $b$, and it is rapid for small $a$, $b$ and slow for large; see Figures 4.12(a) and 4.13(a).

For tests with nonuniform density the situation cardinally changes. The growth of the error is observed only for $a$ and $b$ increasing in the vicinity of zero. For other values of $a$ and $b$ the error is a decreasing function; moreover, if we fix one of $a$

or $b$ large enough and increase the other parameter from small values, then a very rapid decay is observed for both second and fourth order methods; see Figures 4.12(b) and 4.13(b). This is further evidence that the strong singularity gives opportunity for an increase in accuracy by using ANCD. An interesting outcome is also that all of the relative errors obtained using ANCD have the points of the local maximum for small $a = b$. For $N = 30$ these points lie in the approximate interval $a = b \in [5, 10]$.

**4.4. Integration of exponential function over complex domain.** In this section we shall consider the domain that is a half of a ring with center at zero point, $P_r = \{(x, y) : 0 < r < x^2 + y^2 < 1,\ y > 0\}$ (see Figure 4.14), and integrate the function

$$f_3(x, y) = \exp[a(x^2 + y^2)]$$

over this domain. The exact value of the integral of $f_3(x, y)$ over $P_r$ is

$$I(f_3) = \pi \frac{\exp(a) - \exp(ar^2)}{2a}.$$

The direct application of our formulas $Q_\Omega^{\mathrm{tra}}(f)$, $Q_\Omega^{\mathrm{mid}}(f)$, $Q_\Omega^{\mathrm{Ha}}(f)$, $Q_\Omega^{\mathrm{Si}}(f)$ for integrating $f_3(x, y)$ requires us to construct a piecewise linear approximation of the circle boundaries of $P_r$ that leads to passage from integration over $P_r$ to integration over some approximating polygon. Further, this polygon can be decomposed into Voronoi cells. It is worth noting that PolyMesher automatically makes the piecewise linear approximation of boundaries of complex domains (see the enlarged picture in Figure 4.14).

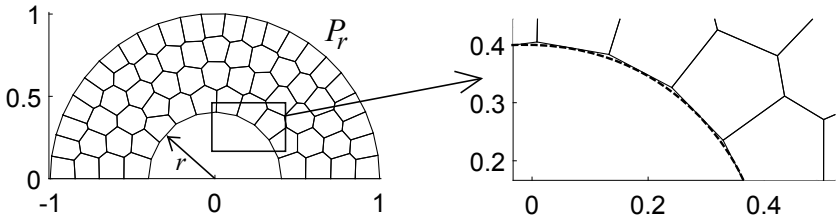


FIG. 4.14. *Half-ring domain with $r = 0.4$, and section lying close to the inner circle.*

One significant disadvantage of such an approximation is that it is exact only if the boundary is described by an affine function that is valid only for polygons. Therefore, for nonpolygonal domains the order of convergence of any cubature formula on polygon meshes is at most two. In our study we are going to enhance this approximation of the boundary, resulting in an increase in the order of convergence for the Simpson formula. By doing so we shall see that all the results of this paper remain valid for the more general case of nonconvex and complex domains. To enhance the approximation after constructing CVTs, we must

(1) find the cells that contain the parts of the circle boundaries of $P_r$ (they lie close to the boundaries);

(2) compute the refined area and coordinates of the center of gravity for these cells, taking into account that they are not polygonal;

(3) for trapezoidal rule, take into account that when applying formula (2.3) for integration over such cells, the integral of $\langle \boldsymbol{x} - \boldsymbol{c}_\Omega, \boldsymbol{n}_i \rangle f(\boldsymbol{x})$ over circle face $S_f$ (not straight face) cannot be expressed as $d(\boldsymbol{c}_\Omega, S_f) \int_{S_f} f(\boldsymbol{x}) d\gamma$. Thus, for integration over

such faces we should use the original expression with the unit outward-pointing normal $\boldsymbol{n}_i(\boldsymbol{x})$ coming from the Green's formula; it is as follows: $\int_{S_f} \langle \boldsymbol{x} - \boldsymbol{c}_\Omega, \boldsymbol{n}_i \rangle f(\boldsymbol{x}) d\gamma$. It must be added to the integrals over straight faces on the right-hand side of (2.3).

**Item 1.** The first of the above items can be easily addressed by checking for each cell whether there is more than one vertex of this cell that lies sufficiently close to the boundary circles. Below we shall denote such polygonal cells by $ABV_3, \ldots, V_n$, assuming that $A$ and $B$ are those vertices (see Figure 4.15). Let us give a bit more detail on implementation of items 2 and 3.

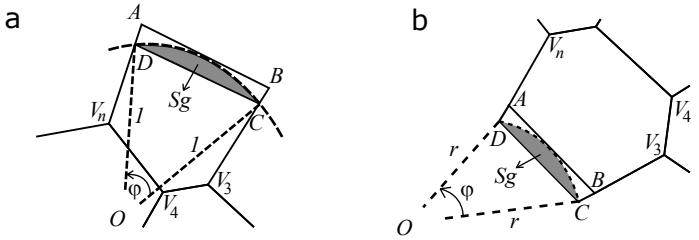


FIG. 4.15. *Cells containing the parts of the circle boundaries and auxiliary constructions:* (a) *cell containing the part of outer circle;* (b) *cell containing the part of inner circle.*

**Item 2.** For the case under consideration there are two possibilities. First is when the cell contains the part of outer circle of the ring (see Figure 4.15(a)); second is when the cell contains the part of inner circle (see Figure 4.15(b)). The parts of the outer and inner circles and their radii are denoted by dash lines. For the first case PolyMesher constructs the polygonal cell $ABV_1, \ldots, V_n$ with the part of the outer circle lying inside the cell. Knowing the coordinates of $V_3$ and $V_n$, we can find the intersection points $C$ and $D$ of lines $V_nA$ and $BV_3$ with the circle. Then we can find the area of sector $OCD$ and the area of triangle $OCD$ and finally obtain the area of filled segment $Sg$ as their difference. The desired refined area of the cell is the sum of areas of polygon $DCV_3, \ldots, V_n$ and of segment $Sg$.

To find the refined coordinates of the center of gravity we used formula (2.1), where in the denominator the refined area should stand, and for computing the numerator we apply the additivity property of the integral combined with the above arguments. It is worth noting here that the integrals of functions $x$ and $y$ over any convex polygon are equal to the corresponding coordinates of the polygon's center of gravity multiplied by its area; see Theorem 2.1 from [9]. The integrals of $x$ and $y$ over circle sectors $OCD$ can be computed after passage to the polar coordinates.

The described method can be applied for the cells lying close to the part of the inner circle, with the only remark being that the desired refined area is the difference of areas of polygon $DCV_3, \ldots, V_n$ and of segment $Sg$. Similar arguments should be used for computing the refined coordinates of the center of gravity.

*Remark* 4.1. Here the method working only for circle boundaries is described. However, we should emphasize that by using parametrization of the boundary curve, a similar method can be developed for any kind of boundary.

**Item 3.** For the cell $\Omega$ with circle faces the trapezoidal rule based on (2.3) is as follows:

$$Q_\Omega^{\mathrm{tra}}(f) = \sum_{F_i \in L} \frac{d(\boldsymbol{c}_\Omega, F_i)}{n} \int_{F_i} f(\boldsymbol{x}) d\gamma_i + \sum_{F_i \in S} \int_{F_i} \langle \boldsymbol{x} - \boldsymbol{c}_\Omega, \boldsymbol{n}_i \rangle f(\boldsymbol{x}) d\gamma_i,$$

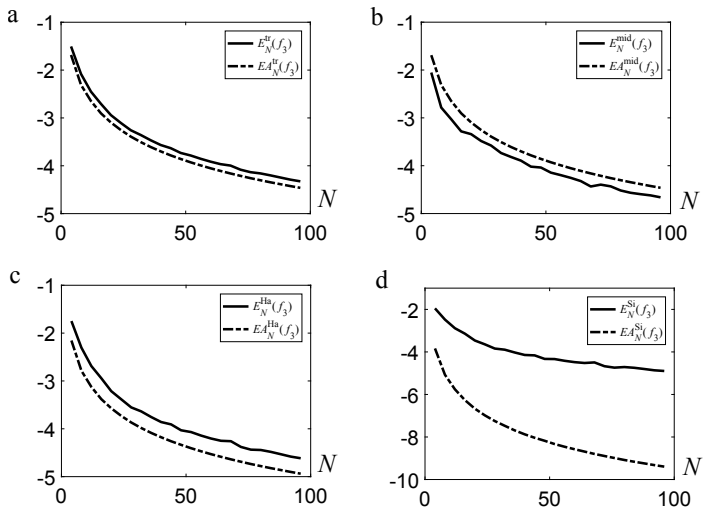


FIG. 4.16. *Common logarithms of the moduli of relative errors obtained while integrating* $f_3(x,y)$ *with* $a = 1$ *and* $r = 0.5$ *using the original (solid line) and the refined (dash line) formulas for the* (a) $Q_\Omega^{\mathrm{tr}}(f_3)$, (b) $Q_\Omega^{\mathrm{mid}}(f_3)$, (c) $Q_\Omega^{\mathrm{Ha}}(f_3)$, *and* (d) $Q_\Omega^{\mathrm{Si}}(f_3)$ *rules.*

where $L$ is the set of straight-line faces of $\Omega$, and $S$ is the set of its non-straight-line faces. Note that we should take the integrals over straight-line faces $V_3C$ and $V_nD$ instead of initial faces $V_3B$ and $V_nA$ (see Figure 4.15). For integration over non-straight-line faces, one should make the parametrization of the boundary. In our case the parameter is angle $\varphi$ and the integrand $\langle \boldsymbol{x} - \boldsymbol{c}_\Omega, \boldsymbol{n}_i \rangle f(\boldsymbol{x})$ is

- $\exp(a)[(\cos\varphi - x_c)\cos\varphi + (\sin\varphi - y_c)\sin\varphi]$ for the case of outer circle,
- $-\exp(ar^2)[(r\cos\varphi - x_c)\cos\varphi + (r\sin\varphi - y_c)\sin\varphi]$ for the case of inner one, where $x_c$, $y_c$ are the refined coordinates of the center of gravity of $\Omega$.

It is worth noting that for all of the one-dimensional integrals over faces, we used the classical Simpson rule, which requires to specify the value of the integrand in the middle point of the segment of integration. Both for straight-line and circle faces these values can be easily found.

Let us denote the relative errors of integration of $f_3(x,y)$ using the original (non-refined) methods by $E_N^{\mathrm{tr}}(f_3)$, $E_N^{\mathrm{mid}}(f_3)$, $E_N^{\mathrm{Ha}}(f_3)$, and $E_N^{\mathrm{Si}}(f_3)$ as in (4.5). The refined methods allow us to obtain more accurate results; their relative errors will be denoted by $EA_N^{\mathrm{tr}}(f_3)$, $EA_N^{\mathrm{mid}}(f_3)$, $EA_N^{\mathrm{Ha}}(f_3)$, and $EA_N^{\mathrm{Si}}(f_3)$ correspondingly. The orders of convergence both for the original and refined methods $R_N^{\mathrm{tr}}(f_3)$, $R_N^{\mathrm{mid}}(f_3)$, $R_N^{\mathrm{Ha}}(f_3)$, and $R_N^{\mathrm{Si}}(f_3)$ are computed as in (4.6).

In Figures 4.16 and 4.17 the errors of integration in the $\log_{10}$ scale are given for the original and refined methods in cases $r = 0.5$, $a = 1$ and $r = 0.5$, $a = 10$. It can be observed that the refined $Q_\Omega^{\mathrm{tr}}(f_3)$ and $Q_\Omega^{\mathrm{Ha}}(f_3)$ rules are more accurate than the original ones. However, a surprising result is that the original midpoint rule turns out to be more accurate than the refined one. The difference between the errors of the original and refined $Q_\Omega^{\mathrm{tr}}(f_3)$ and $Q_\Omega^{\mathrm{Ha}}(f_3)$ rules decreases when increasing the parameter $a$ of function $f_3$ (this parameter defines the values of gradients of $f_3$). Most important is to note that for any values of the parameters, the refined Simpson rule is much more accurate than the original one (see also the results in Tables 4.5 and 4.6).

In Table 4.5 a comparison of the errors of the refined and original methods is given.

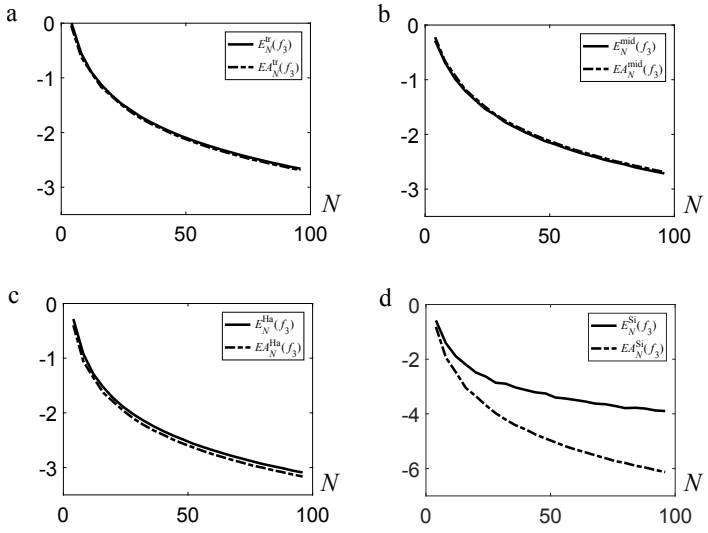


FIG. 4.17. *Common logarithms of the moduli of relative errors obtained while integrating* $f_3(x,y)$ *with* $a = 10$ *and* $r = 0.5$ *using the original (solid line) and the refined (dash line) formulas for the* (a) $Q_\Omega^{\mathrm{tr}}(f_3)$, (b) $Q_\Omega^{\mathrm{mid}}(f_3)$, (c) $Q_\Omega^{\mathrm{Ha}}(f_3)$, *and* (d) $Q_\Omega^{\mathrm{Si}}(f_3)$ *rules.*

TABLE 4.5
*Errors of integration obtained in tests for* $f_3(\boldsymbol{x})$ *with* $a = 2$, $r = 0.5$.

| $N$ | $E_N^{\mathrm{tra}}(f_3)$ | | $E_N^{\mathrm{mid}}(f_3)$ | | $E_N^{\mathrm{Ha}}(f_3)$ | | $E_N^{\mathrm{Si}}(f_3)$ | |
|---|---|---|---|---|---|---|---|---|
| | Refined | Original | Refined | Original | Refined | Original | Refined | Original |
| 4 | -5.48E-02 | -7.82E-02 | 5.3E-02 | 3.5E-02 | -1.89E-02 | -4.05E-02 | -8.93E-04 | -2.16E-02 |
| 8 | -1.42E-02 | -1.87E-02 | 1.41E-02 | 9.96E-03 | -4.79E-03 | -9.16E-03 | -6.07E-05 | -4.38E-03 |
| 16 | -3.63E-03 | -4.74E-03 | 3.63E-03 | 2.47E-03 | -1.21E-03 | -2.34E-03 | -3.88E-06 | -1.14E-03 |
| 32 | -9.05E-04 | -1.15E-03 | 9.04E-04 | 6.53E-04 | -3.02E-04 | -5.52E-04 | -2.38E-07 | -2.50E-04 |
| 64 | -2.26E-04 | -2.77E-04 | 2.26E-04 | 1.76E-04 | -7.55E-05 | -1.26E-04 | -1.44E-08 | -5.03E-05 |
| 128 | -5.65E-05 | -7.06E-05 | 5.65E-05 | 4.25E-05 | -1.88E-05 | -3.29E-05 | -9.E-10 | -1.4E-05 |
| 256 | -1.41E-05 | -1.75E-05 | 1.41E-05 | 1.08E-05 | -4.71E-06 | -8.09E-06 | -5.89E-11 | -3.38E-06 |
| $C_{err}$ | **2.9983** | 2.1263 | **2.9966** | 1.2526 | **1** | 1 | | |
| $C_{err2}$ | 1.2581 | | 0.7389 | | 1.7765 | | 1.56E+04 | |

The data in the last two rows of Table 4.5 is defined as in Table 4.1. It is necessary to note that while computing the integral of convex function $f_3(\boldsymbol{x})$ by the original and refined formulas $Q_P^{\mathrm{tra}}(f_1)$, $Q_P^{\mathrm{mid}}(f_1)$, and $Q_P^{\mathrm{Ha}}(f_1)$, we had been checking inequalities (2.9), (2.14), and (2.16), respectively. Numerical values of the integral often satisfied them. However, the other important theoretical observation concerning the relations between the best constants of the errors of $Q_\Omega^{\mathrm{tr}}(f_3)$, $Q_\Omega^{\mathrm{mid}}(f_3)$, and $Q_\Omega^{\mathrm{Ha}}(f_3)$ rules holds true only for the refined methods, and not for the original ones. Thus, for $n = 2$ the best constants of the errors in the refined $Q_\Omega^{\mathrm{tr}}(f_3)$ and $Q_\Omega^{\mathrm{mid}}(f_3)$ rules coincide and are three times larger than the best constant for the refined $Q_\Omega^{\mathrm{Ha}}(f_3)$ rule.

In Table 4.6 one can observe the orders of convergence for the refined and original formulas and the averaged orders (see the last row). We should underline here that only the refined Simpson rule shows the fourth order. This is caused by an accurate

TABLE 4.6
*Orders of convergence obtained in tests for $f_3(\boldsymbol{x})$ with $a = 2$, $r = 0.5$.*

| $N$ | $E_N^{\mathrm{tra}}(f_3)$ | | $E_N^{\mathrm{mid}}(f_3)$ | | $E_N^{\mathrm{Ha}}(f_3)$ | | $E_N^{\mathrm{Si}}(f_3)$ | |
|---|---|---|---|---|---|---|---|---|
| | Refined | Original | Refined | Original | Refined | Original | Refined | Original |
| 8 | 1.9433 | 2.0634 | 1.9079 | 1.8151 | 1.9774 | 2.1437 | 3.8789 | 2.3016 |
| 16 | 1.9708 | 1.9825 | 1.9615 | 2.0134 | 1.98 | 1.9715 | 3.9688 | 1.9482 |
| 32 | 2.006 | 2.0372 | 2.0037 | 1.9167 | 2.0083 | 2.0822 | 4.0242 | 2.1807 |
| 64 | 1.9991 | 2.0588 | 1.9985 | 1.889 | 1.9997 | 2.1318 | 4.0444 | 2.3154 |
| 128 | 2.0014 | 1.9725 | 2.0012 | 2.0525 | 2.0015 | 1.9366 | 4.0042 | 1.8421 |
| 256 | 2.0003 | 2.0107 | 2.0003 | 1.9829 | 2.0003 | 2.0229 | 3.9329 | 2.054 |
| aver | 1.9868 | 2.0209 | 1.9788 | 1.9449 | 1.9945 | 2.0481 | 3.9756 | 2.107 |

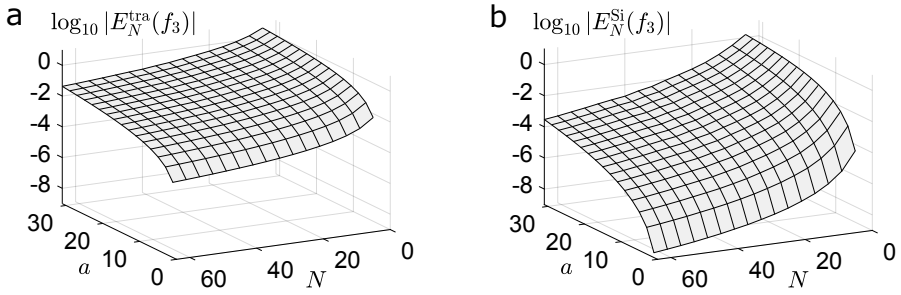


FIG. 4.18. *Common logarithms of the moduli of relative errors obtained while integrating $f_3(x, y)$ with $r = 0.5$ and various values of $a$ using the* (a) *trapezoidal and* (b) *Simpson rules.*

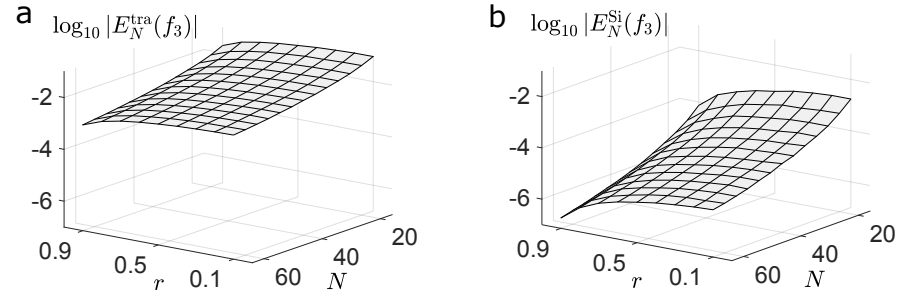


FIG. 4.19. *Common logarithms of the moduli of relative errors obtained while integrating $f_3(x, y)$ with $a = 10$ and various values of $r$ using the* (a) *trapezoidal and* (b) *Simpson rules.*

accounting of the shape of the boundary as described above.

For practical purposes it is also interesting to see how the values of the gradients of the integrand and singularities of the domain of integration can influence the accuracy. To study this question for the case of the integrand and the domain under consideration we give the dependence of the $\log_{10}$ of relative errors on the values of the parameter $a$ (see Figure 4.18) and on the values of the radius $r$ (see Figure 4.19). We obtained correct results for $r = 0.1$, which is a rather small value. To decrease this value further the nonuniform grids should be used.

## REFERENCES


[1] B. Achchab, A. Agouzal, A. Guessab, and Y. Zaim, *An extended family of nonconforming quasi-Wilson elements for solving elasticity problem*, Appl. Math. Comput., 344/345 (2019), pp. 1–19.

[2] M. Bachar and A. Guessab, *Characterization of the existence of an enriched linear finite element approximation using biorthogonal systems*, Results Math., 70 (2016), pp. 401–413.

[3] M. Bachar and A. Guessab, *A simple necessary and sufficient condition for the enrichment of the Crouzeix-Raviart element*, Appl. Anal. Discrete Math., 10 (2016), pp. 378–393.

[4] M. Bachar, A. Guessab, O. Mohammed, and Y. Zaim, *New cubature formulas and Hermite–Hadamard type inequalities using integrals over some hyperplanes in the d-dimensional hyper-rectangle*, Appl. Math. Comput., 315 (2017), pp. 347–362.

[5] E. B. Chin, J. B. Lasserre, and N. Sukumar, *Numerical integration of homogeneous functions on convex and nonconvex polygons and polyhedra*, Comput. Mech., 56 (2015), pp. 967–981.

[6] P. G. Ciarlet, *The Finite Element Method for Elliptic Problems*, North-Holland, Amsterdam, 1978.

[7] M. Crouzeix and P. A. Raviart, *Conforming and non-conforming finite element methods for solving the stationary Stokes equations*, RAIRO Anal. Numer., 7 (1973), pp. 33–76.

[8] Q. Du, V. Faber, and M. Gunzburger, *Centroidal Voronoi tessellations: Applications and algorithms*, SIAM Rev., 41 (1999), pp. 637–676, https://doi.org/10.1137/S0036144599352836.

[9] A. Guessab and G. Schmeisser, *Convexity results and sharp error estimates in approximate multivariate integration*, Math. Comp., 73 (2004), pp. 1365–1384.

[10] A. Guessab and B. Semisalov, *A multivariate version of Hammer's inequality and its consequences in numerical integration*, Results Math., 73 (2018), 33.

[11] A. Guessab and B. Semisalov, *Numerical integration using integrals over hyperplane sections of simplices in a triangulation of a polytope*, BIT, 58 (2018), pp. 613–660.

[12] A. Guessab and Y. Zaim, *A unified and general framework for enriching finite element approximations*, in Progress in Approximation Theory and Applicable Complex Analysis, Springer Optim. Appl. 117, Springer, Cham, 2017, pp. 491–519.

[13] J. S. Hesthaven and T. Warburton, *Nodal Discontinuous Galerkin Methods. Algorithms, Analysis, and Applications*, Texts Appl. Math. 54, Springer-Verlag, New York, 2008.

[14] J. B. Lasserre, *Integration on a convex polytope*, Proc. Amer. Math. Soc., 12 (1998), pp. 2433–2441.

[15] A. Ouazzi and M. Turek, *Unified edge-oriented stabilization of nonconforming FEM for incompressible flow problems: Numerical investigations*, J. Numer. Math., 15 (2007), pp. 299–322.

[16] C. Talischi, G. Paulino, A. Pereira, and I. F. M. Menezes, *Polymesher: A general-purpose mesh generator for polygonal elements written in Matlab*, Struct. Multidisc. Optim., 45 (2012), pp. 309–328.